



The regulation of Lewis acid/basic sites in NaFe bimetal MOXs for the controllable photocatalytic degradation of electron-rich/deficient VOCs

Lu Chen ^{a,b,c}, Xiao Wang ^{a,*}, Gansheng Shi ^a, Guanhong Lu ^a, Yan Wang ^a, Xiaofeng Xie ^a, Deliang Chen ^{b,c,**}, Jing Sun ^{a,*}

^a State Key Lab of High Performance Ceramics and Superfine Microstructure, Shanghai Institute of Ceramics, Chinese Academy of Sciences, 585 Heshuo Road, Shanghai 201899, China

^b Research Institute of Interdisciplinary Science & School of Materials Science and Engineering, Dongguan University of Technology, Dongguan 523808, China

^c School of Materials Science and Engineering, Zhengzhou University, Zhengzhou 450001, China



ARTICLE INFO

Keywords:

Lewis acid/basic sites
NaFe-MOXs
Sodium benzoate
O-xylene
Acetaldehyde

ABSTRACT

The performance of metal-organic xerogels (MOXs) in the photocatalytic oxidative degradation (PCO) of volatile organic compounds (VOCs) relies on their Lewis acid-base interaction and the generation of oxidative radicals. Herein, by engineering the local charge imbalance of carboxyl ligands through synthesizing NaFe bimetal MOXs, the Lewis acidity of MIL-100(Fe) MOX was well tuned for the adsorption-degradation of electron-rich (aromatic hydrocarbons) and electron-deficient (aldehydes) VOCs. Benefiting from the implanted Lewis basic sites, NaFe-MOXs showed increased adsorption-PCO capacity for single acetaldehyde, while Fe-MOX with abundant Lewis acid sites could capture and degrade more o-xylene. The Lewis basic sites promoted the mineralization of single o-xylene and acetaldehyde by altering their interactions with the photocatalysts and improving the generation of oxidative radicals, which extended the lifetime of photocatalysts. By regulating the Lewis acid/basic sites within MOXs, this work provides an effective way for optimizing photocatalysts to enable the photocatalytic degradation of both electron-rich/deficient VOCs.

1. Introduction

In the recent decades, many efforts have been made to solve the problem of massive emissions of VOCs into air [1–3]. Photocatalytic technology is considered as an effective means to remove VOCs due to its low energy consumption, mild reaction conditions and easy to be implemented [4–8]. Metal-organic frameworks (MOFs), constructed by metal ions (or metal clusters) and organic ligands, have attracted extensive interests in adsorption and separation [9], gas sensing [10], water purification [11–13], CO₂ reduction [14], especially in the capture and photocatalytic conversion of VOCs due to their high specific surface area and semiconductor-like photocatalytic activity [15–18]. However, despite the high specific surface area, most MOFs reported previously, such as MIL-100 and MIL-101, show micropores with average diameters of less than 2 nm, which is not conducive to the migration of guest molecules to active sites, further hindering the photocatalytic reaction [19–21]. Therefore, in recent years, MOFs with

hierarchical pores have been proven to be a new research trend in the photocatalytic elimination of VOCs.

Metal-organic xerogels (MOXs) is a kind of monolithic MOFs with hierarchical pores, in which MOF nanoparticles with diameters of several nanometers are assembled into 3-D frameworks through weak hydrogen bonds, π-π stacking, and Van Der Waals [22,23]. MOXs, as a new kind of functional materials, have shown great potential in the development of high-performance electrochemical sensors, superhydrophobic materials, ion storage devices, drug delivery and highly sensitive analytical measurement due to their inherent hierarchical microporous/mesoporous structure [24–26]. Mahmood and co-workers synthesized AlFe bimetallic MOGs with enhanced adsorption of Rhodamine B and methyl orange by chemisorption [27]. Berke et al. [28] fabricated a gel by Al³⁺ ions and 1,4,5,8-trptycenedetracarboxylic acid, which showed maximum fluorescence quenching ability for the detection of picric acid with a detection limit of 5–10 ppb. Li et al. [29] prepared various Al-MOGs by gelation of Al³⁺ ions with different

* Corresponding authors.

** Corresponding author at: Research Institute of Interdisciplinary Science & School of Materials Science and Engineering, Dongguan University of Technology, Dongguan 523808, China.

E-mail addresses: wangxiao@mail.sic.ac.cn (X. Wang), dlchen@zzu.edu.cn (D. Chen), jingsun@mail.sic.ac.cn (J. Sun).

carboxylic acids in the ethanol solution to adsorb H₂ and CO₂, and separate CO₂ from N₂ and CH₄. Compared with crystalline MOFs, the mesoporous characteristic of MOXs improves the gas migration rate and reduces the diffusion resistance of VOCs molecules to reach the catalytic sites [22,30]. Zhang et al. [31,32] prepared granular Al-based MOXs by a facile way, which exhibited outstanding performance for the capture of toluene and p-xylene under wet conditions, much higher than BPL activated carbon, zeolite 13X, and some representative MOFs. At present, the organic ligands used in most MOXs reported are polyphenyl carboxylic acids, which can adsorb aromatic VOCs through π-π interaction. Meanwhile, metal-oxygen clusters in MOXs often act as Lewis acid centers to trap electron-rich aromatic VOCs [4,33]. Compared with crystalline MOFs, MOXs usually exhibit more Lewis acid sites due to the exposure of unsaturated coordinated metal atoms. In our previous work, we synthesized hierarchically porous MIL-100(Fe) MOF/MOX homojunctions by adjusting the type of anions (NO₃⁻ and Cl⁻) in metal precursors and confirmed that the coordinatively unsaturated acid Fe₃O sites could facilitate the capture of electron-rich BTXS (benzene, toluene, xylenes and styrene) molecules and showed high photocatalytic activity towards the degradation of BTXS [34]. Despite the promoted adsorption, mass transfer and PCO of BTXS, the performance of MIL-100 (Fe) MOF/MOX in the capture of electron-deficient oxygenated VOCs like aldehydes were quite poor due to the single type of Lewis acid sites. As most oxygenated VOCs with electron deficiency tend to interact with Lewis basic sites of photocatalysts. Therefore, the implantation of Lewis basic sites would be essential for trapping and degrading aldehydes. Shang et al. [35] fine-tuned the structure of ZIF-8 to form electron-rich isocyanate groups (Lewis basic sites) in ZIF-8-T via a facile thermal treatment, showing around 2.1 and 9.4 times the HCHO adsorption capacity and photocatalytic degradation efficiency of pristine ZIF-8, respectively. Despite all those efforts, the implantation of Lewis basic sites into the Lewis acid MOXs to realize the controllable photocatalytic degradation of both aromatic VOCs and oxygenated VOCs is a challenging problem, being worthy of investigation.

Many efforts have been devoted to achieve the regulation of Lewis acid/basic sites of MOFs. The implantation of guest metal ions with lower charge-balancing ability into MOFs has been regarded as an effective way in introducing Lewis basic sites. Zeng et al. [36] created Lewis basic sites within an anionic defective MOF by the concerted interactions between the pendant carboxylate groups, embedded Pd NPs and charge-balancing cations. Hou et al. [37] achieved the introduction of Na⁺/K⁺ into MOF, which not only changed the size and geometry of the metal clusters, but also regulated the acidity of the pore surface. Although the centers of alkali metal ion show strong bonding with ligand carboxylic acid groups due to their high charge density, most implantation methods rely on the post-synthetic treatments, and it is still a challenge to introduce cations into MOXs through facile one-step methods. Besides, most of the previous works concentrated on the influences of Lewis acid/basic sites on the adsorption of gas molecules, the role of these sites in the photocatalytic oxidation (PCO) of VOCs is still unclear, which limits the purposefully design of Lewis acidity/basicity of MOX photocatalysts.

In this work, we developed Na-Fe bimetal MOXs with adjustable Lewis acid/basic sites. Based on the divergence of charge-balancing ability of various metal centers, the local charge imbalance of ligands was achieved, which activated the carboxyl groups into the Lewis basic sites [36,38]. By controlling the dosage of C₇H₅NaO₂ regulator, 0.5NaFe-MOX, 1NaFe-MOX and 3NaFe-MOX with tunable Lewis acid/basic sites were prepared through a one-pot synthesis process. On the basis of these NaFe-MOXs, the controllable photocatalytic degradation of electron-rich o-xylene (a typical aromatic VOCs) and electron-deficient acetaldehyde (a typical oxygenated VOCs) were achieved. The roles of Lewis acid/basic sites in the adsorption and PCO of various VOCs were analyzed through adsorption experiments, TPD and *in-situ* DRIFTS. Finally, the PCO mechanisms of both aromatic and oxygenated VOCs were proposed.

2. Experimental section

2.1. Materials

Iron nitrate nonahydrate (Fe(NO₃)₃·9H₂O), sodium benzoate (C₇H₅NaO₂), trimesic acid (H₃BTC) and N, N-dimethylformamide (DMF) were provided by Shanghai Adamas Reagent Co., Ltd. 5,5-dimethyl-1-pyrroline N-oxide (DMPO) was produced by Sigma Chemical Co., Ltd. 2,2,6,6-tetramethyl-1-piperidinyloxy (TEMPO) and p-benzoquinone (p-BQ) were produced by Sigma-Aldrich. Ethanol was purchased from Sinopharm Chemical Reagent Co., Ltd. Ultrapure water machine (Tondino Scientific (Shanghai) Co., Ltd) was used to prepare deionized water for the experiments.

2.2. The preparation of materials

2.2.1. The synthesis of Fe-MOX

1 mmol of Fe(NO₃)₃·9H₂O was dissolved in 25 mL of DMF. The mixed solution was magnetically stirred for 12 h. 1 mmol of H₃BTC was then added into the mixed solution, continuously stirring for 1 h. The mixed solution was then transferred into a stainless-steel reactor with a polytetrafluoroethylene lining of 100 mL, which was heated in an oven at 150 °C for 12 h and cooled to room temperature to obtain Fe-MOG (Metal-organic gels). After being washed with DMF and ethanol, Fe-MOG was dried in vacuum at 60 °C for 16 h to obtain Fe-MOX.

2.2.2. The preparation of NaFe-MOXs

1 mmol Fe(NO₃)₃·9H₂O was dissolved in 25 mL DMF. 0.5 mmol C₇H₅NaO₂ was slowly added into the solution of Fe(NO₃)₃·9H₂O. The mixture was stirred for 12 h to ensure that the C₇H₅NaO₂ was completely dissolved in the solution. 1 mmol H₃BTC was then added into the above solution under continuously stirring for 1 h. Finally, the mixture was then transferred to a stainless-steel autoclave with a 100 mL polytetrafluoroethylene liner, heated at 150 °C for 12 h, and cooled to room temperature to obtain 0.5NaFe-MOG. After being washed by DMF and ethanol through centrifugation, the wet 0.5NaFe-MOG was vacuum dried at 60 °C for 16 h to obtain 0.5NaFe-MOX. By changing the amount of C₇H₅NaO₂ to 1 mmol and 3 mmol, 1NaFe-MOX and 3NaFe-MOX were synthesized, respectively.

2.3. Characterization

X-ray diffraction patterns were collected on a Power X-ray diffraction (PXRD, Bruker D8 advanced diffractometer) with Cu-Kα radiation over the 2θ range of 3–70° at a scanning rate of 2 °/min. Fourier Transform Infrared spectra (FTIR) and Raman spectra were analyzed by Microscopic infrared spectrometer (Thermo Scientific Vertex 70, USA) and Raman microscopy (Thermo Scientific DXR, USA) to achieve structure information of the samples. X-ray photoelectron spectroscopy (XPS) analysis was performed with a SCAlab250 instrument (USA) using Al Kα monochromatic X-ray radiation source. Field emission scanning electron microscopy (SEM) tests were carried out on a Magellan 400 instrument (USA) equipped with energy dispersive X-ray spectroscopy (EDS) were used to study the microstructure and elemental composition of the samples. Nitrogen adsorption-desorption isotherms of the materials were tested on a BET Surface Area Analyzer (Quadasorb SI, USA). UV-Vis diffuse reflectance spectra measurements were performed on a Perkin Elmer Lambda 1050 (USA) to research the optical absorbance behavior of the materials. Photoluminescence spectroscopy measurements were carried out on a Perkin Elmer instrument (USA) to obtain the information on electrons and holes of the samples with the excitation wavelength at 320 nm. The electrochemical experiments were measured on a CHI 650b (CH Instrument Company, Shanghai, China) electrochemical workstation equipped with a standard three-electrode system to characterize the transient photocurrent and Mott-Schottky (M-S) plots of the materials at room temperature. Electron spin resonance (ESR)

experiments were performed on a JES-FA200 instrument (Japan) to characterize the active radicals of the materials. The acidity/basicity of the samples, as well as the adsorption behavior of target molecules were measured by a Temperature-programmed desorption (TPD) instrument (ChemiSorb PCA-1200, Bibuilder, China) with NH₃, CO₂, or target VOCs (o-xylene or acetaldehyde) as the probe molecule, respectively. Details of the TPD characterizations were found in the [Supporting information](#). A gas chromatography (GC) with a flame ionization detector (FID) detector made in Beijing China Education Au-light Co., Ltd. was used to detect the concentration of o-xylene and acetaldehyde during the adsorption and photocatalytic degradation. A GC-FID with a nickel catalyst accessory for transforming low-level CO₂ to methane was applied to measure the concentration of CO₂ produced during the photocatalytic degradation of o-xylene and acetaldehyde. Details were found in the [Supporting information](#). *In-situ* Diffuse Reflection Infrared Fourier Transform (DRIFT, Shimadzu IRTtracer-100, Japan) spectra and GC-MS (GCMS-QP2010Ultra, Shimadzu) were carried out to analyze the intermediates of the photocatalytic degradation of o-xylene and acetaldehyde.

2.4. Adsorption and photocatalysis performance of Fe-MOX and NaFe-MOXs

As shown in [Scheme S1](#), home-made reaction system containing gas mixing unit, photocatalytic reaction chamber, and GC monitoring unit was used to study the adsorption and photocatalysis performance of Fe-MOX and NaFe-MOXs at room temperature. In the gas mixing unit, air generated by a nitrogen-hydrogen-air integrated machine was injected into a humidification tank to carry water into the reaction chamber. The relative humidity (RH) was kept at 60% by tuning the flow rate of air and the content of water in the humidification tank to simulate atmosphere environment. The velocity of air, o-xylene or acetaldehyde were controlled at 10 sccm by gas flowmeters. The humidified air was blended with o-xylene or acetaldehyde in the gas mixing unit before flowing into the reaction chamber. The concentration of o-xylene and acetaldehyde was set as 25 ppm and 500 ppm, respectively. The sample (50 mg) was dispersed in ethanol and coated on a glass plate (12 × 5 cm). After being dried at 60 °C for 1 h, the sample was placed in the reaction chamber (15 × 8 × 1 cm). A Xenon lamp acted as the light source was placed 30 cm above the reaction chamber. The saturated adsorption capacity ($C_{\text{adsorption}}$, μmol/g) of o-xylene or acetaldehyde was computed according [Eq. I](#).

$$C_{\text{adsorption}} = \frac{c_0 \times \rho_0 \times \rho_1 \times \left\{ \left(\int_0^t v \times c dt \right)_{\text{blank}} - \left(\int_0^t v \times c dt \right)_{\text{sample}} \right\}}{M \times m} \quad (\text{I})$$

where c_0 (ppm) and c represent the initial and real-time concentration of polluted gas at a specific time interval, respectively. ρ_0 (g/cm³) and ρ_1 stand for air density and relative density of VOCs at ambient temperature. v (mL/min) is the total real-time velocity of air and polluted gas, and t (min) is the time point of data recorded by GC. M (g/mol) represents the molar mass of polluted gas. m (g) is the mass of photocatalyst applied during the reaction. The photocatalytic removal ratio (η) of polluted gas was calculated according to [Eq. II](#).

$$\eta = (1 - c/c_0) \times 100\% \quad (\text{II})$$

3. Result and discussion

3.1. Characterization of morphology of NaFe-MOXs

The micro-morphology of the samples and the distribution of elements in 0.5NaFe-MOX were studied by SEM-EDS. As shown in [Fig. 1a](#) and b, Fe-MOX displayed a flat surface with small pores, in accordance

with MIL-100(Fe) xerogel reported previously [39]. No obvious difference was observed in the SEM images of 0.5NaFe-MOX and 1NaFe-MOX compared with Fe-MOX. However, when the amount of C₇H₅NaO₂ increased to 3 mmol, the pores in the flat surface of 3NaFe-MOX ([Fig. 1g](#) and h) were more obvious than that of Fe-MOX, which was probably attributed to the increase of alkalinity of the synthesis system caused by C₇H₅NaO₂ hindering the coordination between Fe and BTC³⁺. The EDS results in [Fig. 1i, j, and k](#) demonstrated that Fe, C, and O were uniformly distributed in 0.5NaFe-MOX. Moreover, EDS analysis and inductively coupled plasma emission spectrometer (ICP-OES, [Table S1](#)) results confirmed that the implantation of Na into Fe-MOX could be adjusted according to different C₇H₅NaO₂ feeding ratio. However, the concentration of Na in the results of ICP-OES was obviously lower than that of the Fe, although the concentration of Na added reached 3 times of that of Fe in the synthesis process. The reason for the result is that the coordination between Na⁺ and deprotonated BTC³⁺ is difficult to form MOXs due to the lack of available empty orbit in Na⁺ compared with Fe³⁺ [40, 41]. Therefore, during the formation NaFe-MOXs, deprotonated BTC³⁻ would preferentially coordinate with Fe³⁺ while Na⁺ could only partially replace the coordination of Fe³⁺.

3.2. The synthesis mechanism of NaFe-MOXs

The synthesis of NaFe-MOXs was illustrated in [Scheme 1](#). As shown in [Fig. S1](#), with the addition of C₇H₅NaO₂, the color of Fe(NO₃)₃·9H₂O solution gradually changed from bright red to dark red, which might be attributed to the coordination between Fe³⁺ in Fe(NO₃)₃·9H₂O and the carboxylic acid groups in C₇H₅NaO₂. When H₃TBC was added, Na⁺ in C₇H₅NaO₂ would coordinate with carboxylic acid groups in H₃TBC and partially replace the coordination of Fe³⁺. Due to the different charge-balancing ability of Na⁺ and Fe³⁺, the electron density of carboxylic acid group in the organic ligands of NaFe-MOXs was enhanced, which resulted in the generation of Lewis basic sites. A gel-state product was obtained after the solvothermal reaction when C₇H₅NaO₂ less than 3 mmol was introduced, while precipitations were found when the content of C₇H₅NaO₂ reaching 3 mmol ([Fig. S2](#)). The phenomena were probably attributed to the increase of alkalinity of the solution with the addition of C₇H₅NaO₂, which perturbed the self-assembly of nanocrystals into Fe-MOG [42].

3.3. Characterization of composition and Lewis acid/basic sites of NaFe-MOXs

The crystal structure of the samples was analyzed by PXRD. In [Fig. 2a](#), the XRD pattern of Fe-MOX matched well with the simulated XRD of MIL-100(Fe) ([Fig. S3](#)) [10,43]. New peaks at 10.2°, 17.6°, 20.3°, 24.3°, 26.1°, 27.2°, 28.0°, 33.3°, 35.7°, and 37.2° gradually appeared with the addition of C₇H₅NaO₂ from 0.5 mmol to 3 mmol, which was probably attributed to the partial coordination of Na⁺ in C₇H₅NaO₂ with BTC³⁺. Despite the observation of new peaks, NaFe-MOXs showed similar primary crystal structure as Fe-MOX, implying that the introduction of Na⁺ did not destroy the intrinsic crystal structure of Fe-MOX. In addition, the results of FTIR and Raman spectra ([Fig. 2b and S4](#)) also confirmed that the structure of NaFe-MOXs was consistent with Fe-MOX in the molecular level [10]. The electronic state and coordination of Fe atoms in NaFe-MOXs were researched by XPS. As shown in [Fig. S5](#), XPS survey spectra of NaFe-MOXs confirmed the coexistence of Fe, C, O, and Na, which agreed well with the EDS mapping results. Compared with Fe-MOX (726.1 eV, 58.1% calculated by the peak area), a slight decrease of 0.3 and 0.5 eV in the binding energy of Fe 2p1/2 for 1NaFe-MOX (725.8 eV, 40.6%) and 3NaFe-MOX (725.6 eV, 23.5%) happened, respectively, indicating an increase in the electron density of Fe species due to the coordination of carboxyl groups in C₇H₅NaO₂ with Fe ([Fig. 2c](#)) [44]. As shown in [Fig. 2d](#), three kinds of oxygen species were observed from the deconvoluted spectra of O 1 s. The peak at 532.1 eV corresponded to the undisturbed carboxylate groups in the secondary

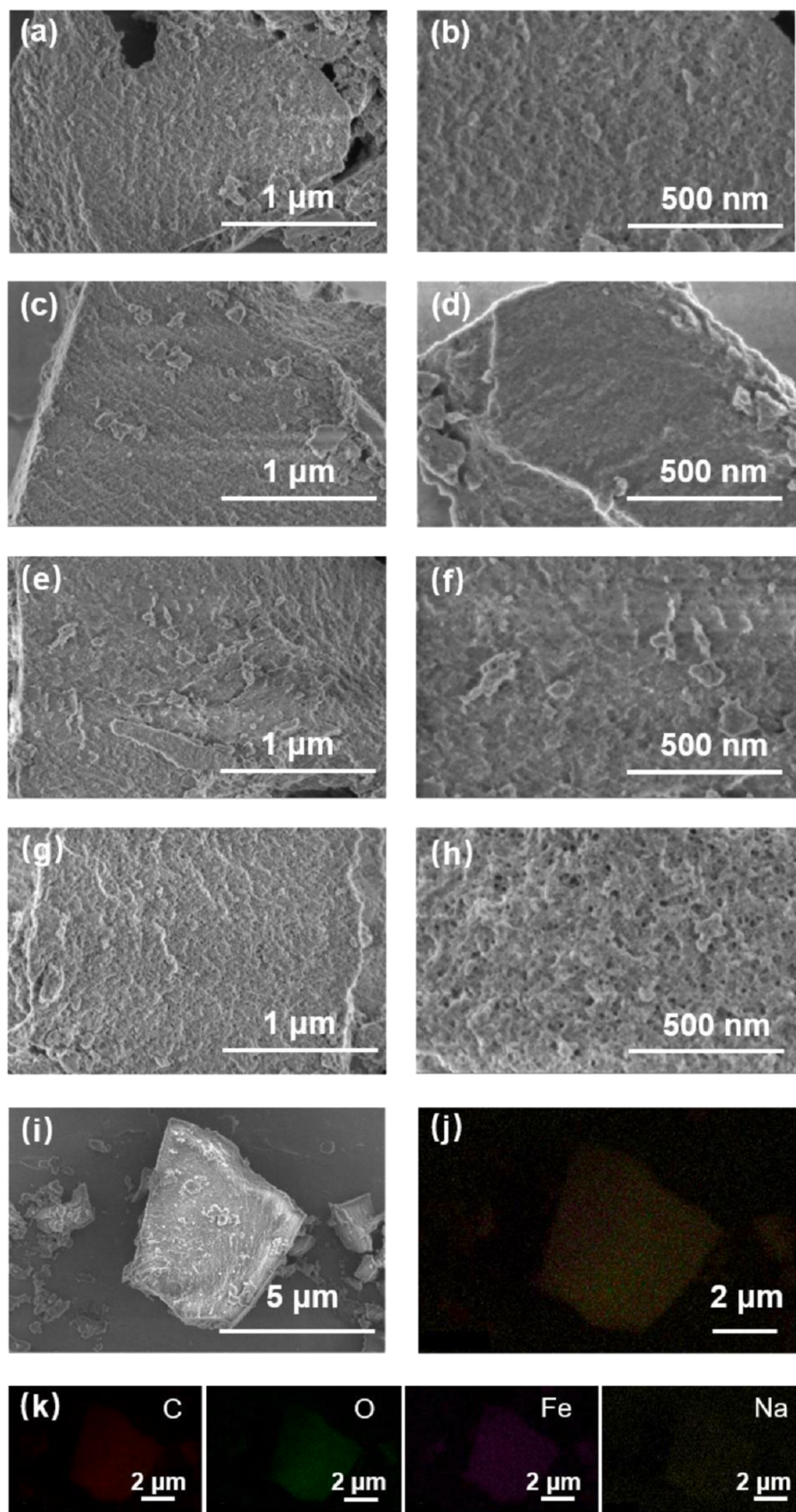
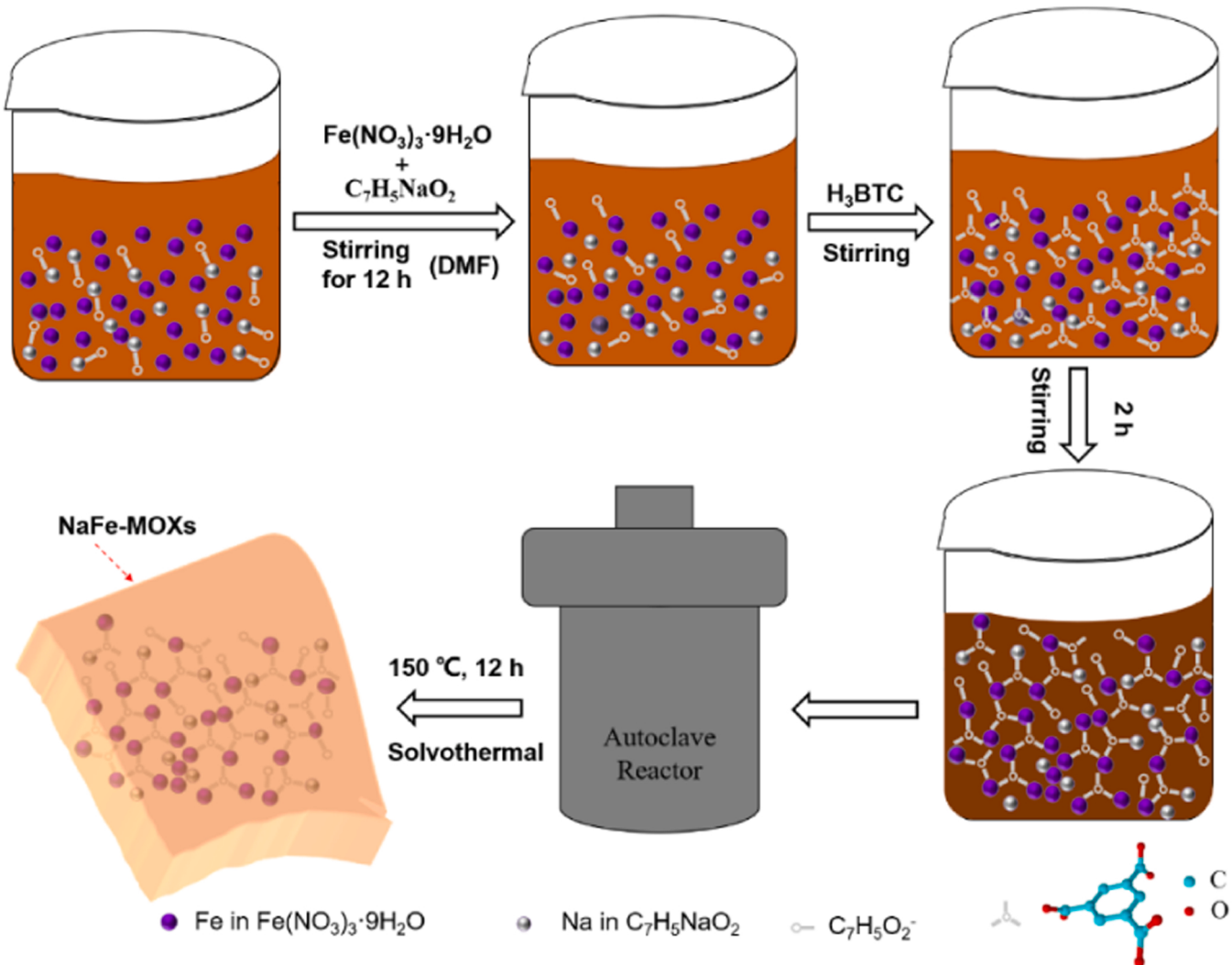


Fig. 1. (a-h) SEM images of (a-b) Fe-MOX, (c-d) 0.5NaFe-MOX, (e-f) 1NaFe-MOX, (g-h) 3NaFe-MOX; (i-k) EDS mappings of C, O, Fe and Na elements of 0.5NaFe-MOX.



Scheme 1. The diagram for the synthesis mechanism of NaFe-MOXs.

building units (SBU, C-O-Fe) of Fe-MOX. The weak shoulder peak at 533.5 eV was assigned to H_2O adsorbed [36]. Compared with Fe-MOX (10.1%), the intensity of peaks for H_2O adsorption increased in all the NaFe-MOXs (0.5NaFe-MOX~25.3%, 1NaFe-MOX~18.8%, and 3NaFe-MOX~20.4%) as a result of the hydrogen bond formed between the electron-rich oxygen atom in the linkers of NaFe-MOXs and water. A red-shift in the peak for adsorbed H_2O was observed in 1NaFe-MOX and 3NaFe-MOX. Similar to the results reported by Zeng et al. [36] the O 1 s peak assigned to carboxylate groups (COO^-) at 531.9 eV gradually shifted to 531.6 eV with the introduction of Na^+ . Meanwhile, the peaks at 286.4 eV and 288.9 eV assigned to C-O and C=O in the deconvoluted spectra of C 1s of NaFe-MOXs shifted to lower binding energy compared with that of Fe-MOX (Fig. 2e). The red-shift of O 1s and C 1s peaks indicated an increase of the electron density on the carbonyl oxygen, which was related to the relatively lower electron affinity of Na^+ compared with Fe^{3+} as charge-balancing species. The unbalanced charge localization of perturbed carboxylate groups enabled the activation of carboxylate groups to act as Lewis basic sites [36].

The amount of Lewis acid/basic sites in Fe-MOX and NaFe-MOXs was further verified by NH_3/CO_2 -FTIR and CO_2 -DRIFT spectra. As shown in the NH_3 -FTIR spectra (Fig. 3a), the peak at 3164 cm^{-1} corresponding to the asymmetrical stretching vibration of N-H bonds ($\nu_{as}\text{N-H}$) was observed in both Fe-MOX and NaFe-MOXs, which indicated the existence of Lewis acid sites [45]. Fig. 3b gives the CO_2 -DRIFT spectra. Compared with Fe-MOX, the peak at 1355 cm^{-1} corresponding to the

symmetrical stretching vibration of C-H bond ($\nu_{as}\text{C-H}$) shifted to higher wavenumber, which was attributed to the increased electron density of O atom in the carboxylate groups, confirming an increase in the Lewis basicity of the carboxylate groups in NaFe-MOXs. The same phenomenon was observed in the CO_2 -FTIR (Fig. S6). The introduction of Na^+ into Fe-MOX activated the perturbed carboxylate groups by charge mismatch to generate Lewis basic sites for the adsorption of CO_2 [37]. An additional peak at 1635 cm^{-1} (Fig. 3b) was observed in NaFe-MOXs after the adsorption of CO_2 , which was assigned to the ν_{as} of carbonate ion owing to the O-CO₂ interaction [46]. In addition, NH_3/CO_2 -TPD were also applied to analyze the Lewis acid/basic sites in Fe-MOX and NaFe-MOXs. Three peaks were observed in the NH_3 -TPD results (Fig. 3c), which were divided into weak (~110 °C), first medium (224–243 °C), and second medium (287–296 °C) acid sites according to the classification criteria given by Topsøe et al. [47]. In Fig. 3c, the peak assigned to the weak acid sites in the samples gradually weakened with the introduction of Na^+ , while the peak for first medium acid sites in Fe-MOX gradually changed from 224 °C to 243 °C. The peaks for second medium acid sites shifted from 296 °C (Fe-MOX) to 287 °C (0.5NaFe-MOX) and disappeared in 1NaFe-MOX and 3NaFe-MOX. Since the peak intensity in NH_3 -TPD is proportional to the amount of Lewis acid sites in the samples, these results confirmed the relatively lower acidity of NaFe-MOXs compared to Fe-MOX. On one hand, the coordination with $(\text{C}_7\text{H}_5\text{O}_2)^-$ from $\text{C}_7\text{H}_5\text{NaO}_2$ lowered the amount of unsaturated Fe atoms, which were important Lewis acid sites in Fe-MOX. On the other hand,

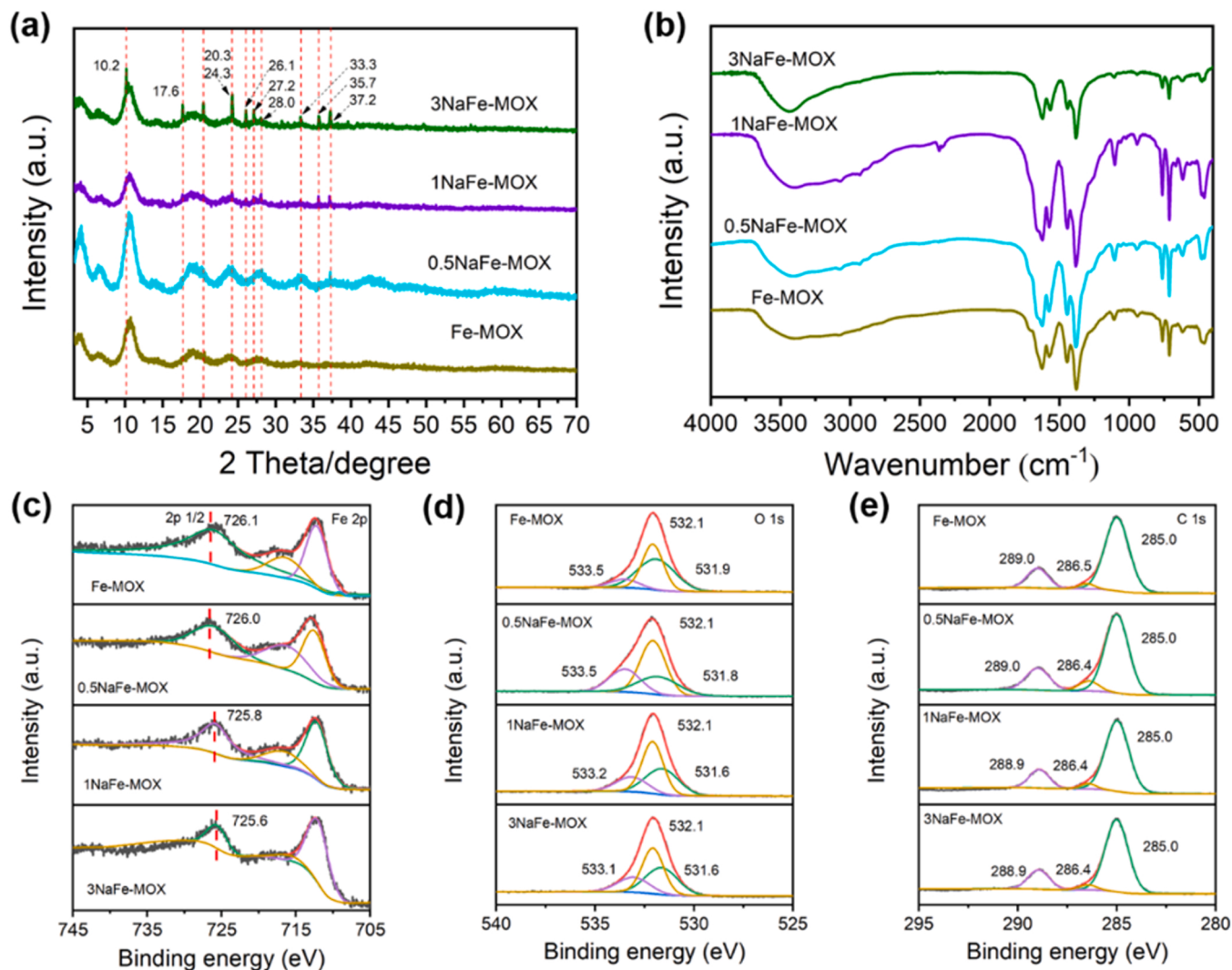


Fig. 2. (a) XRD patterns and (b) FTIR spectra of Fe-MOX and NaFe-MOXs; (c-e) The deconvolution of XPS spectra of (c) Fe 2p, (d) O 1s, and (e) C 1s in Fe-MOX and NaFe-MOXs.

the partial replacement of Fe by Na further lowered the amount of Lewis acid sites. Fig. 3d gives the CO₂-TPD results. The peak for moderately strong basic sites gradually shifted from 228 °C (Fe-MOX) to 246 °C (3NaFe-MOX), demonstrating an increase in the basic sites with the increasing content of Na⁺ in NaFe-MOXs. The results combined with the XPS analysis indicated the successful adjustment of Lewis acid/basic sites in NaFe-MOXs.

3.4. Characterization of photoelectric properties

Aside from the Lewis acidity, the performance of the photocatalysts is also determined by their ability in using incident light. Despite the introduction of Na⁺, NaFe-MOXs showed excellent light absorption behavior in the ultraviolet and visible regions (Fig. 4a). As shown in Fig. 4b, the band gap energy of Fe-MOX, 0.5NaFe-MOX, 1NaFe-MOX, and 3NaFe-MOX was calculated as 2.64, 2.66, 2.67, and 2.68 eV, respectively. In Fig. 4c, 0.5NaFe-MOX, 1NaFe-MOX showed decreased PL intensities with respect to Fe-MOX, confirming that the recombination of photogenerated electron-hole was effectively inhibited. As reported by Aubrey et al., the coordination between carboxylic acid groups in H₃BTC and Na⁺ in NaFe-MOXs would result in the variety of split energy levels, which could explain the reduced recombination of photogenerated electron-hole pairs and the decreased PL intensity [48]. Similar trend was observed in the photocurrent response results

(Fig. 4d). 0.5NaFe-MOX, 1NaFe-MOX showed much higher photocurrent responses than Fe-MOX, indicating the effective separation and transfer of photogenerated carriers to participate in photocatalytic reactions. However, the introduction of excessive C₇H₅NaO₂ increased the alkalinity of the solution, which hindered the coordination of Fe³⁺ with the carboxyl acid group in H₃BTC and led to the formation of defects. In addition, more Na⁺ participated in the coordination with carboxylic acid groups in H₃BTC instead of Fe³⁺, further resulting in defects and partial structural collapse of 3NaFe-MOX (Fig. 2a). The defects in 3NaFe-MOX might work as recombination centers for photogenerated electrons and holes and result in the relatively higher PL intensity and lower photocurrent response than 0.5NaFe-MOX and 1NaFe-MOX. Despite the increased recombination of photogenerated electron-hole pairs, 3NaFe-MOX still showed higher photocurrent intensity than Fe-MOX, confirming that the appropriate addition of C₇H₅NaO₂ into Fe-MOX was beneficial to the separation and migration of photogenerated carriers.

As important oxidative species for the degradation of o-xylene and acetaldehyde, the generation of hydroxyl (·OH) and superoxide (·O₂) radicals has been regarded as an important index when evaluating the performance of photocatalysts. As shown in Fig. 5a and b, 0.5NaFe-MOX showed the strongest signal of ·OH among these four samples, while 1NaFe-MOX and Fe-MOX gave strong ·O₂ signals. In order to further explain this phenomenon, Mott-Schottky (M-S) plots and HOMO-XPS

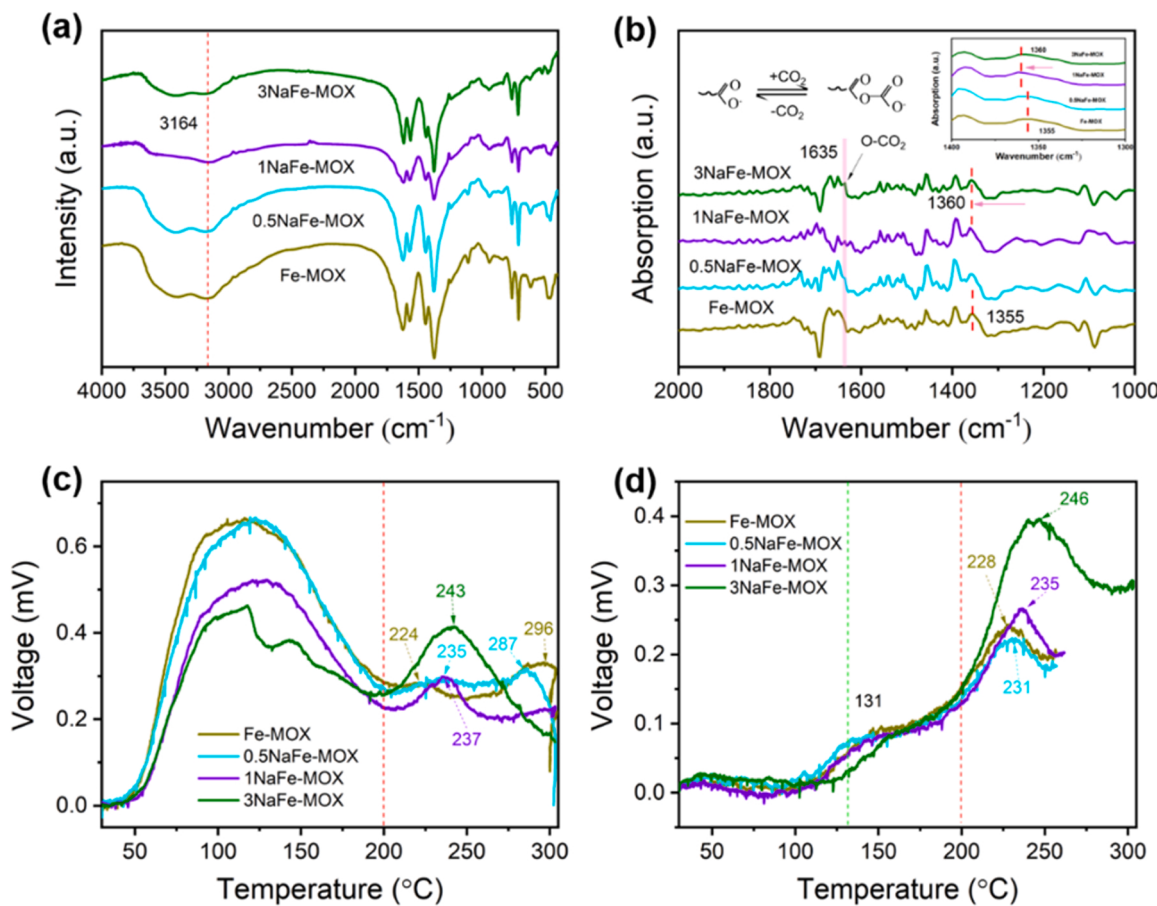


Fig. 3. FTIR spectra of Fe-MOX and NaFe-MOXs after adsorption of NH₃; (b) Comparison of DRIFT spectra of Fe-MOX and NaFe-MOXs after adsorption of CO₂; (c-d) Temperature-programmed desorption (TPD) of (c) NH₃ and (d) CO₂ in Fe-MOX and NaFe-MOXs.

spectra of Fe-MOX and NaFe-MOXs were tested. All of the M-S plots showed a positive slope, indicating that Fe-MOX and NaFe-MOXs were all n-type semiconductors (Fig. 5c) [49,50]. The flat band potentials (E_{fb}) of Fe-MOX, 0.5NaFe-MOX and 1NaFe-MOX were equivalent to -0.38 , -0.51 and -0.52 V vs. normal hydrogen electrode (NHE), respectively. The Fermi level (E_f) of the samples was therefore defined since E_f is usually closed to E_{fb} . The HOMO XPS spectra (Fig. 5d) displays the energy gap from the HOMO maximum to E_f (E_{ho-f}) of Fe-MOX and NaFe-MOXs [45,51]. Therefore, E_{ho-f} of Fe-MOX, 0.5NaFe-MOX, and 1NaFe-MOX was measured to be 2.42, 2.44, and 2.47 eV vs. NHE, respectively. According to the value of E_{ho-f} and E_f , the HOMO orbital energy levels (E_{ho}) of Fe-MOX, 0.5NaFe-MOX and 1NaFe-MOX were calculated as 2.04, 1.93, and 1.95 V, respectively (Eq. III). Thus, the LUMO orbital energy levels (E_{lu}) of Fe-MOX, 0.5NaFe-MOX, and 1NaFe-MOX, were calculated as -0.60 , -0.73 and -0.72 V, respectively, according to Eq. IV.

$$E_{ho} = E_f + E_{ho-f} \quad (\text{III})$$

$$E_g = E_{ho} - E_{lu} \quad (\text{IV})$$

As shown in Fig. 5e, photo-induced holes in the HOMO states of NaFe-MOXs were not sufficient for the oxidation of OH[·]/OH (1.99 eV vs. NHE). As reported by Langford et al. [52], under light irradiation, the transformation of Fe₃O₄(OH) to Fe(II) and ·OH would happen through an inner ligand-metal charge transfer (LMCT) process (Fig. 5e). Therefore, the promoted generation of Fe₃O₄(OH) due to the existence of Lewis basic sites in NaFe-MOXs might be the main reason for the increased concentration of ·OH [53]. Another possible reason for generating ·OH was the activation and sequence reduction of absorbed O₂ by

photo-generated electrons. (O₂ → O₂[·] → H₂O₂ → ·OH, Equation S2~S4) [54]. The ·OH and O₂[·] produced together with the Lewis acid/basic sites participated in the photocatalytic degradation of acetaldehyde and o-xylene [55,56].

3.5. The adsorption performance and adsorption mechanism

In order to check the possibility of NaFe-MOXs in the controllable photocatalytic degradation of electron-rich/deficient VOCs, o-xylene and acetaldehyde were used to represent electron-rich and electron-deficient VOCs as target pollutants, respectively. An adsorption test was firstly carried out to investigate the influence of Lewis acid/basic sites of NaFe-MOXs on their adsorption capacity towards o-xylene and acetaldehyde. As shown in Fig. S7a and b, when the photocatalysts were used, the concentration of o-xylene and acetaldehyde were both much lower than those of the blank chamber, confirming that o-xylene and acetaldehyde molecules were both effectively adsorbed by the samples. The adsorption capacity of the samples for o-xylene and acetaldehyde was calculated by Equation I (Fig. 6a). Fe-MOX showed the highest adsorption capacity (26.09 μmol/g) for o-xylene. The adsorption capacity of NaFe-MOXs for o-xylene gradually decreased to ~9.14 μmol/g (0.5NaFe-MOX), ~5.00 μmol/g (1NaFe-MOX), and ~0.97 μmol/g (3NaFe-MOX). In the purpose of understanding the adsorption capacity, BET analysis was applied to study the N₂ isotherms and pore-structure of Fe-MOX and NaFe-MOXs. As shown in Table S2, the specific surface areas of Fe-MOX, 0.5NaFe-MOX, 1NaFe-MOX and 3NaFe-MOX corresponded to 615, 407, 554 and 387 m²/g, respectively. All the samples showed type-IV N₂ isotherm curves, with a sharp rise before P/P₀ = 0.1 and the H2-type hysteresis loops in the high P/P₀ region, indicating the

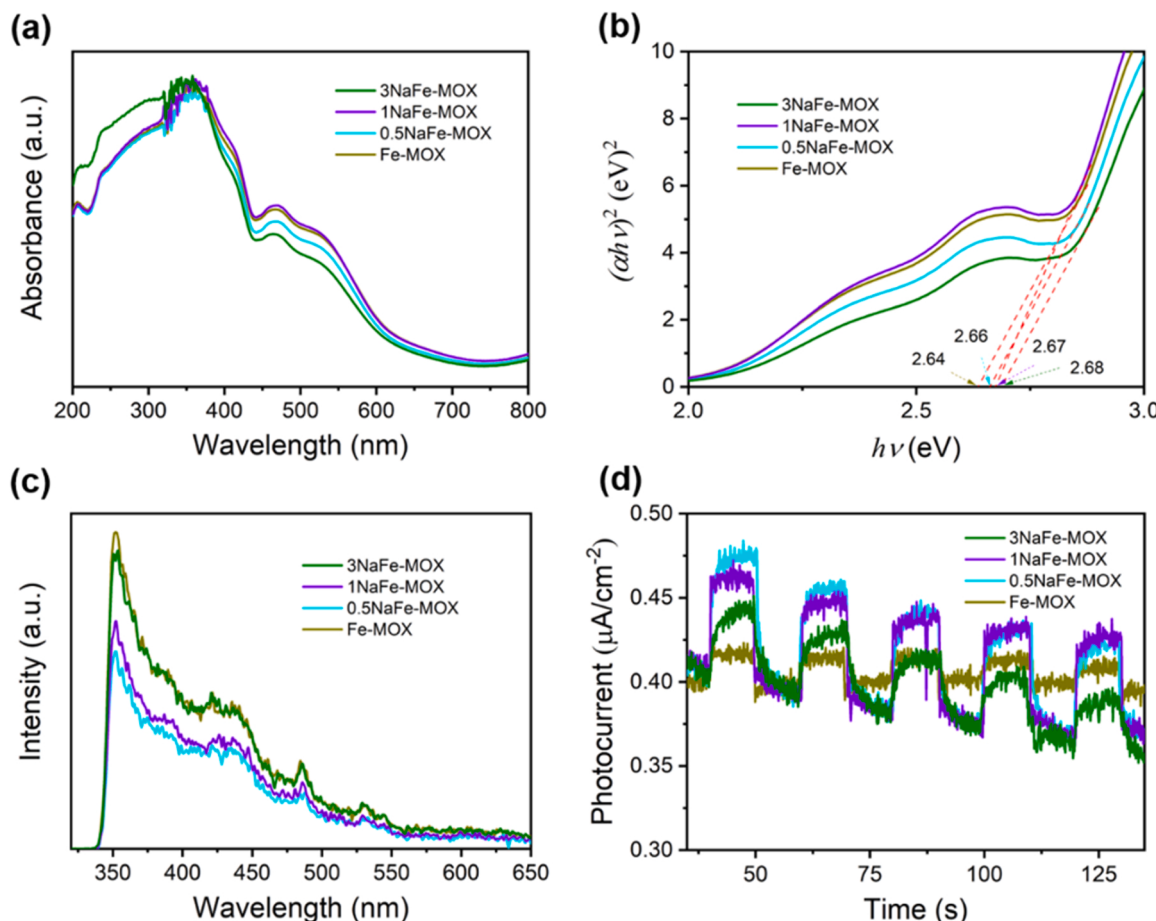


Fig. 4. (a) Diffuse reflectance spectroscopy, (b) the plots of $(\alpha h\nu)^2$ vs photon energy ($h\nu$), (c) photoluminescence spectroscopy, (d) photocurrent response of Fe-MOX, 0.5NaFe-MOX, 1NaFe-MOX, 3NaFe-MOX.

existence of both micro- and mesopores (Fig. 6b and Fig. S8) [19,29], which benefited the adsorption and mass transfer of o-xylene. The high adsorption capacity of Fe-MOX for o-xylene was mainly attributed to its high specific surface area and large amount of acid sites, while the adsorption capacity of NaFe-MOXs for o-xylene gradually decreased due to their reduction of specific surface areas and acid sites. Although the specific surface area of 1NaFe-MOX ($554 \text{ m}^2/\text{g}$) was higher than that of 0.5NaFe-MOX ($407 \text{ m}^2/\text{g}$), its adsorption capacity for o-xylene ($5.0 \mu\text{mol/g}$) was much lower than that of 0.5NaFe-MOX ($9.14 \mu\text{mol/g}$), which indicated that the Lewis acid sites played an essential role in the adsorption electron-rich o-xylene [57,58]. Fig. 6c shows the adsorption capacity of acetaldehyde by the samples. Fe-MOX displayed the highest adsorption capacity ($1.91 \mu\text{mol/g}$) for acetaldehyde. As reported by Sun et al. [59], unsaturated coordinated metal atoms acted as active sites for the adsorption of acetaldehyde by interacting with carbonyl oxygen, while methyl hydrogen in acetaldehyde formed hydrogen-bond with adjacent oxygen in the ligands (noted as Fe-acetaldehyde interaction). This was accounted for the high adsorption of acetaldehyde by Fe-MOX. The specific surface area of 3NaFe-MOX was the smallest, but the adsorption capacity of acetaldehyde ($1.27 \mu\text{mol/g}$) was equivalent to that of 0.5NaFe-MOX, indicating that the increase of Lewis basic sites was also favorable for the adsorption of electron-deficient acetaldehyde. In addition to the Fe-acetaldehyde interaction, as discussed in the XPS results, the Lewis basic sites (carboxyl acid groups with improved electron density) and the existence of Na^+ enabled the formation of -OH groups, which could form hydrogen-bond with carbonyl oxygen in acetaldehyde (noted as H-bond interaction). To verify the positive role of Lewis basic sites, the adsorption behavior of acetaldehyde on Fe-MOX and NaFe-MOXs was further analyzed with TPD. As shown in Fig. 6d,

two desorption peaks at 140 and 149°C were found in 0.5NaFe-MOX and 1NaFe-MOX, respectively, which was attributed to the H-bond adsorption of acetaldehyde by Lewis basic sites. Another peak at 233°C due to the Fe-acetaldehyde interaction was observed and the intensity of the peak in Fe-MOX was the highest, consistent with the highest adsorption capacity ($1.91 \mu\text{mol/g}$) of acetaldehyde. The corresponding desorption temperatures of 0.5NaFe-MOX, 1NaFe-MOX and 3NaFe-MOX for acetaldehyde increased to 238 , 241 , and 237°C , respectively, confirming that the existence of Lewis basic sites increased the binding ability to acetaldehyde. As a consequence of the decreased surface area and the blockage of active Fe sites by $\text{C}_7\text{H}_5\text{O}_2^-$, reduced peak intensities of NaFe-MOXs was observed. Benefiting from the difference on the Lewis acid/basic sites, NaFe-MOXs showed tunable adsorption capacity towards electron-rich o-xylene and electron-deficient acetaldehyde.

3.6. Photocatalytic performance and degradation mechanism

After achieving the adsorption equilibrium, the following photocatalytic experiments were carried out with a Xenon lamp as the light source to verify the influence of the Lewis acidity of the samples on their performance in the photocatalytic degradation of o-xylene and acetaldehyde. The photocatalytic degradation efficiencies of o-xylene and acetaldehyde were repeated three times and computed by Eq. II. As displayed in Fig. 7a, the degradation efficiency of o-xylene by Fe-MOX (67.9%) was higher than NaFe-MOXs ($0.5\text{NaFe-MOX} \sim 47.7\%$, $1\text{NaFe-MOX} \sim 33.8\%$, and $3\text{NaFe-MOX} \sim 13.5\%$) under the irradiation of a 250 W Xenon lamp corresponding light intensity of $31 \text{ mW}/\text{cm}^2$. However, the degradation efficiency of o-xylene by Fe-MOX gradually

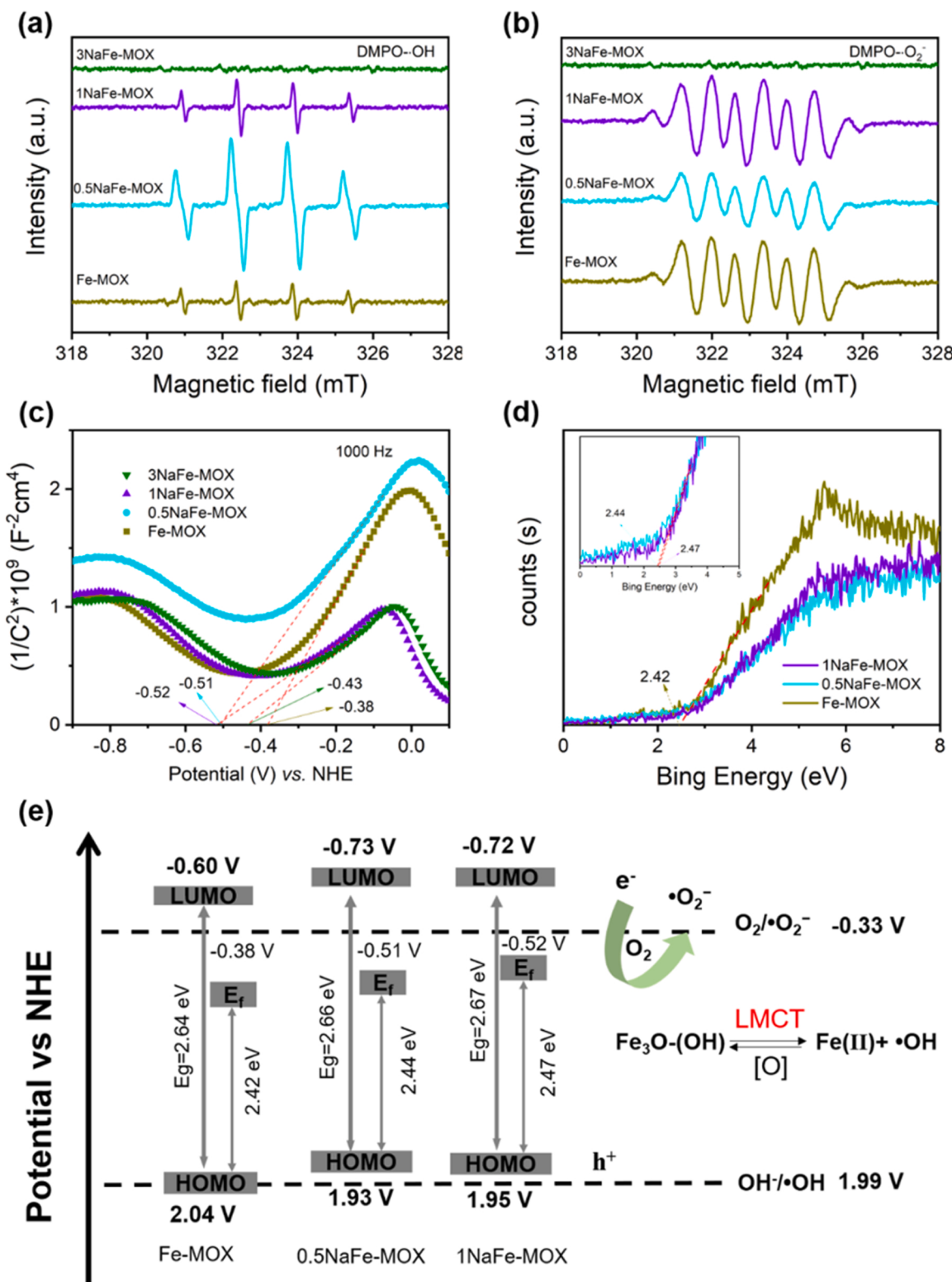


Fig. 5. (a-b) DMPO spin-trapping ESR spectra for (a) the •OH in H₂O (b) the •O₂ in ethanol of Fe-MOX and NaFe-MOXs; (c) Mott-Schottky plots and (d) HOMO-XPS spectra of Fe-MOX and NaFe-MOXs; (e) Schematic illustration of the estimated energy band structures of Fe-MOX and NaFe-MOXs.

descended and deactivation happened after 70 min, while NaFe-MOXs still kept the original photocatalytic activity for o-xylene. This high performance of Fe-MOX was probably attributed to the effective adsorption of electron-rich o-xylene by abundant Lewis acid sites [60, 61]. As shown in Fig. 7b, unlike the circumstance of o-xylene, 0.5NaFe-MOX and 1NaFe-MOX exhibited better performance in the degradation

of acetaldehyde with the PCO efficiencies of 35.6% and 38.0%, respectively, higher than that of Fe-MOX (23.5 %) under the irradiation of a 500 W Xenon lamp corresponding light intensity of 40 mW/cm². However, when the addition of C₇H₅NaO₂ reached 3 mmol, the degradation efficiency of 3NaFe-MOX for acetaldehyde decreased to 22.6%. Although the enhancement of basic sites in NaFe-MOXs promoted the

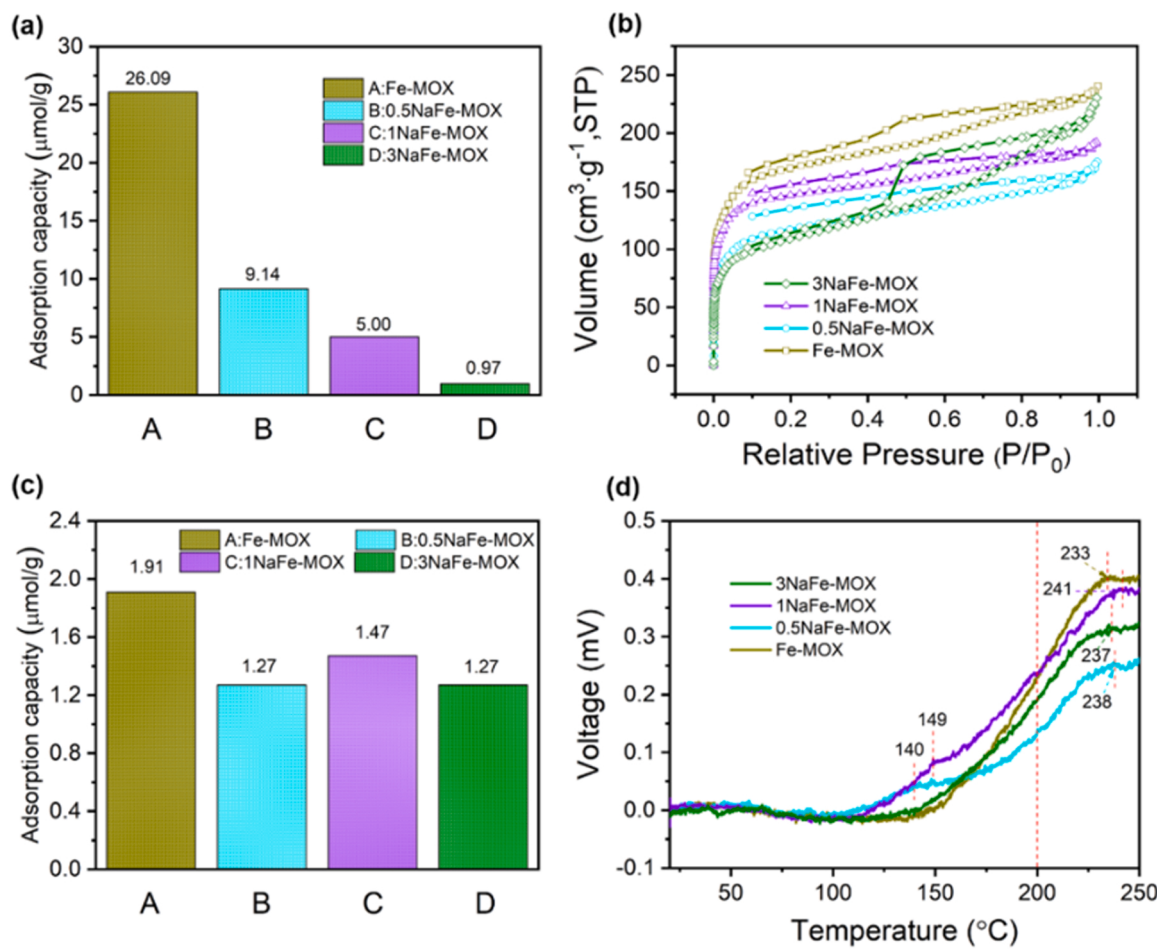


Fig. 6. The saturated adsorption capacity of the as-prepared materials (50 mg) in the airflow of (a) o-xylene molecules (25 ppm) and (b) acetaldehyde molecules (500 ppm); (c) N_2 adsorption-desorption isotherms of Fe-MOX and NaFe-MOXs; (d) Temperature-programmed desorption (TPD) for acetaldehyde of Fe-MOX and NaFe-MOXs.

adsorption of acetaldehyde, the introduction of excessive Na was unfavorable for the generation of $\cdot\text{OH}$ and $\cdot\text{O}_2^-$. The kinetics of photocatalytic degradation depend on time evaluated by the pseudo-first-order kinetic model were shown in Fig. S9. Fe-MOX exhibited the highest reaction rate (0.00202 min^{-1}) in Fig. S9a, in accordance with its high performance in the PCO of o-xylene. 0.5NaFe-MOX displayed a reaction rate of 0.00026 min^{-1} in the degradation of acetaldehyde, which was equal to that of 1NaFe-MOX and 3.25 times that of Fe-MOX (Fig. S9b). As discussed above, by tuning the acidity of Fe-MOX, the photocatalytic performance of electron-rich o-xylene and electron-deficient acetaldehyde was well regulated. The concentration of CO_2 was detected to investigate the effect of Lewis acid/basic sites of the samples on the mineralization of VOCs. As shown in Fig. 7c, almost no CO_2 was detected during the photocatalytic degradation of o-xylene by Fe-MOX while the concentration of CO_2 detected maintained at about 12 ppm when 0.5NaFe-MOX was applied. Similar phenomenon was also observed during the photocatalytic degradation of acetaldehyde. The concentration of CO_2 generated by 1NaFe-MOX was significantly higher than that of Fe-MOX in the PCO of acetaldehyde. Due to high specific surface area and porous structure of Fe-MOX and NaFe-MOXs, CO_2 generated during the early stage of the reaction was trapped in the pore channels of the photocatalysts and was not be detected. As the reaction proceeded, more CO_2 was generated until the adsorption of CO_2 by the photocatalysts reached saturation. The CO_2 generated subsequently escaped into the gas phase and then was detected by GC. Therefore, CO_2 was observed after some time in Fig. 7c and d. According to our previous report, CO_2 generated during the PCO of VOCs was adsorbed by Fe-MOF, which

made the measured CO_2 concentration lower than the actual production value [34]. In the purpose of eliminating the influence of CO_2 -adsorption, the photocatalysts were sealed in dark for 12 h to allow the desorption of adsorbed CO_2 and Fig. 7e and f showed the concentration of CO_2 detected afterwards. The concentration of CO_2 adsorbed by 0.5NaFe-MOX and 1NaFe-MOX during photocatalytic degradation of o-xylene and acetaldehyde was both higher than by Fe-MOX. The mineralization rates of 0.5NaFe-MOX and 1NaFe-MOX for o-xylene and acetaldehyde were 50.0% and 36.2%, respectively, calculated by the Equation S5. Therefore, NaFe-MOXs effectively promoted the photocatalytic mineralization of VOCs, which was probably attributed to the positive role of Lewis basic sites. The stability of Fe-MOX and 1NaFe-MOX as photocatalysts was then tested through cyclic PCO of o-xylene and acetaldehyde. As shown in Fig. S10a and b, the removal efficiency of Fe-MOX for o-xylene remained at 65%, while the removal efficiency of 1NaFe-MOX for acetaldehyde remained at 38% after 3 cycles. Compared with of pristine Fe-MOX and 1NaFe-MOX, no obvious variation was observed in FTIR spectrum collected after 3 cycle tests, indicating the structure of Fe-MOX and 1NaFe-MOX remained unchanged (Fig. S10c and d).

In order to explore the influence of Lewis acid/basic sites on the degradation paths of o-xylene and acetaldehyde, *in-situ* DRIFT spectra were collected to detect the intermediates on Fe-MOX and NaFe-MOXs during the adsorption and photocatalytic degradation processes. Fig. 8a and b displays the adsorption and degradation of o-xylene by Fe-MOX and 0.5NaFe-MOX. As shown in Fig. 8a, with the introduction of o-xylene, peaks (Table S3) assigned to the benzene ring of o-xylene

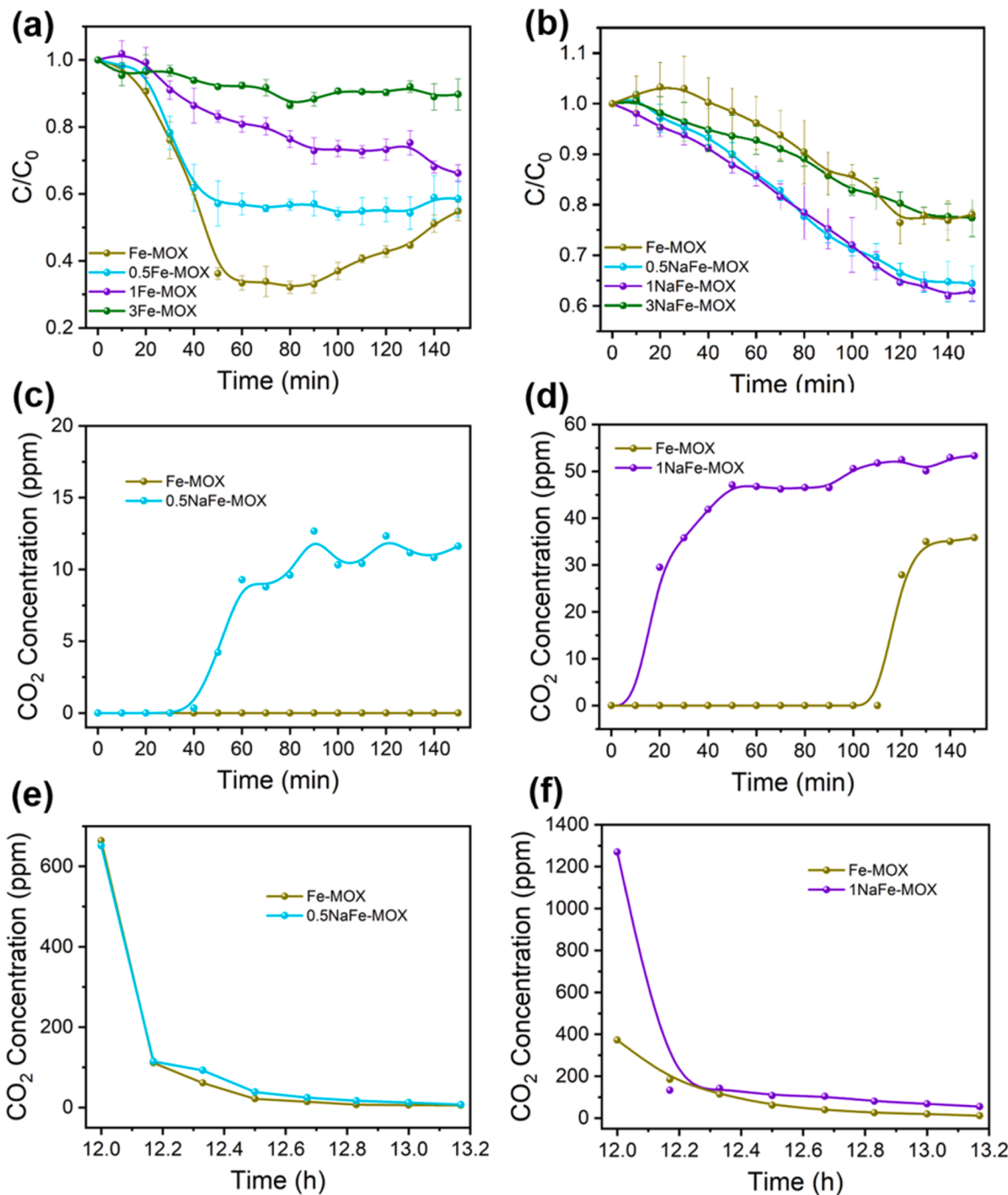


Fig. 7. The photocatalytic degradation efficiencies of (a) o-xylene (25 ppm) under a 250 W Xenon irradiation and (b) acetaldehyde (500 ppm) under a 500 W Xenon irradiation for Fe-MOX and NaFe-MOXs; (c) The change of \$\text{CO}_2\$ concentrations detected during the photocatalytic degradation of o-xylene by Fe-MOX and 0.5NaFe-MOX; (d) The change of \$\text{CO}_2\$ concentrations detected during the photocatalytic degradation of acetaldehyde by Fe-MOX and 1NaFe-MOX; The concentration change of \$\text{CO}_2\$ adsorbed by the samples during the photocatalytic degradation of (e) o-xylene and (f) acetaldehyde.

appeared at once [62–65]. The bands for benzyl aldehydes (\$1690 \text{ cm}^{-1}\$) also appeared and became intense as the adsorption proceeded, which inferred that the \$\alpha\$-H of o-xylene firstly reacted with the \$\text{Fe}_3\text{O}(\text{OH})\$ catalytic sites on Fe-MOX to form benzyl aldehydes via a neutralization reaction [63]. After starting the light irradiation, the band assigned to o-xylene (\$1000 \text{ cm}^{-1}\$) descended, while the bands at 1200 and \$1690 \text{ cm}^{-1}\$ (benzyl aldehydes) became more and more intense, confirming the oxidation of adsorbed o-xylene into benzyl aldehydes by active free radicals generated by Fe-MOX. Unlike the circumstance of Fe-MOX, only relatively weak bands for aromatic ring (\$1510 \text{ cm}^{-1}\$) and benzyl aldehydes (\$1695 \text{ cm}^{-1}\$) appeared during the adsorption of

o-xylene by 0.5NaFe-MOX photocatalyst (Fig. 8b), which was in accordance with its relative poor adsorption capacity towards o-xylene (Fig. 6a). Upon switching on the Xenon lamp, the band for benzyl aldehyde (\$1695 \text{ cm}^{-1}\$) became inconspicuous and the intensities of the bands for carboxylic groups (\$1735\$ and \$926 \text{ cm}^{-1}\$) [66,67] gradually enhanced, confirming the successive ring-opening of benzyl aldehydes by NaFe-MOXs. As indicated by the ESR results, the amount of \$\cdot\text{OH}\$ generated was significantly increased by the introduction of \$\text{Na}^+\$. \$\cdot\text{OH}\$ radicals was found to be essential for the ring-opening and mineralization of xylene and its derivatives [68]. In addition, GC-MS was used to identify the intermediates in the PCO of o-xylene by 0.5NaFe-MOX as

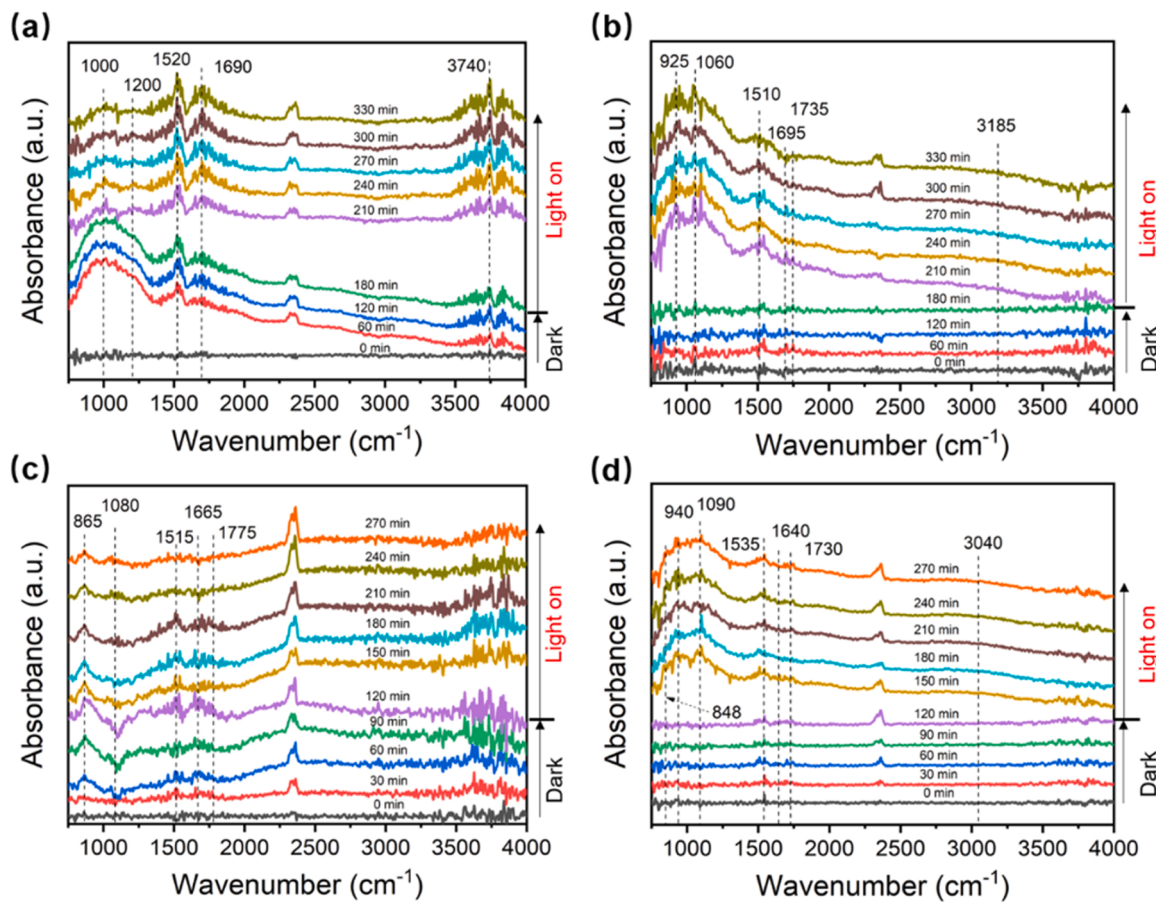


Fig. 8. The *in-situ* DRIFT spectra of (a) Fe-MOX and (b) 0.5NaFe-MOX during adsorption and photocatalytic degradation of o-xylene; The *in-situ* DRIFT spectra of (c) Fe-MOX and (d) 1NaFe-MOX adsorption and photocatalytic degradation of acetaldehyde.

shown in Table S4 and Fig. S11. C_8H_{10} (m-xylene), C_9H_{12} (cumene), $\text{C}_8\text{H}_8\text{O}$ (m-tolualdehyde) and C_9H_{20} (n-nonane) were found due to the attack by h^+ , $\cdot\text{OH}$ and $\cdot\text{O}_2^-$ radicals. Therefore, 0.5NaFe-MOX showed better mineralization ability and stability for the PCO of o-xylene. Through the formation sequence of these intermediates, it could be conjectured that o-xylene first adsorbed onto the surface of Fe-MOX and 0.5NaFe-MOX and reacted with $\text{Fe}_3\text{O}-(\text{OH})$ catalytic sites to generate benzyl aldehyde, which was oxidized to benzoic acids by 0.5NaFe-MOX and was ultimately mineralized into CO_2 and H_2O by $\cdot\text{OH}$ and $\cdot\text{O}_2^-$ radicals.

Fig. 8c and d showed the DRIFT spectra collected during the adsorption and photocatalytic degradation of acetaldehyde by Fe-MOX and 1NaFe-MOX (Table S5). During the adsorption of acetaldehyde by Fe-MOX (Fig. 8c), the band at 1665 cm^{-1} assigned to the stretching vibration of $\text{C}=\text{O}$ in acetaldehyde was found, indicating that the molecular acetaldehyde was adsorbed on the surface of the Fe-MOX. After turning on the Xenon lamp, the intensity of the band for $\text{C}=\text{O}$ in acetaldehyde gradually decreased. New bands related to the stretching vibration of $\text{C}-\text{OH}$ in ethanol (1080 cm^{-1}) were observed, indicating the formation of ethanol as an intermediate during the mineralization of acetaldehyde by Fe-MOX, which was attributed to the electron and proton transfer between unsaturated coordinated Fe (acid sites) and acetaldehyde [69]. When 1NaFe-MOX was applied as the photocatalyst (Fig. 8d), the band corresponded to the stretching vibration of $\text{C}-\text{OH}$ in ethanol (1090 cm^{-1}), strong bands for $\text{O}-\text{H}$ in aliphatic carboxylic acid (940 cm^{-1}) and $\text{C}=\text{O}$ in aliphatic carboxylic acid (1730 cm^{-1}) emerged immediately after the Xenon lamp was turned on, confirming the formation of both ethanol and aliphatic carboxylic acid intermediates. Aside from the acetaldehyde-Fe interaction, H-bond would also form between carbonyl oxygen in acetaldehyde and the hydroxyl groups in

NaFe-MOXs. The proton transfer under light irradiation through the H-bond between -OH groups on NaFe-MOXs and carbonyl oxygen in acetaldehyde might be the key reason for the oxidation of acetaldehyde into aliphatic carboxylic acid, a key intermediate for the fully mineralization of acetaldehyde into CO_2 and H_2O . Besides, in order to further study the reaction mechanism of 1NaFe-MOX photocatalytic degradation of acetaldehyde, the intermediates were identified by GC-MS as shown in Table S6 and Fig. S12. The peak of $\text{C}_3\text{H}_6\text{O}_2$ (propionic acid) was detected with the high relative abundance (6.44%), which was also consistent with the results of *in-situ* DRIFTS that acetaldehyde molecules tended to transform into aliphatic carboxylic acids combined with Lewis basic sites. Based on the above analysis, it could be speculated that acetaldehyde first adsorbed on the surface of Fe-MOX and 1NaFe-MOX, and ethanol was generated by the electron and proton transfer between $\text{Fe}_3\text{O}-(\text{OH})$ and acetaldehyde. H-bond in 1NaFe-MOX made acetaldehyde convert to aliphatic carboxylic acid by the proton transfer under light irradiation and finally be mineralized into CO_2 and H_2O by active oxygen radicals.

In order to evaluate the effects of $\cdot\text{OH}$ and $\cdot\text{O}_2^-$ on the degradation efficiency, the *in-situ* trapping experiments for OH and $\cdot\text{O}_2^-$ were performed. 2,2,6,6-tetramethyl-1-piperidinyloxy (TEMPO) and *p*-benzoquinone (*p*-BQ) were applied as scavengers to trap $\cdot\text{OH}$ and $\cdot\text{O}_2^-$ for the PCO of o-xylene and acetaldehyde, respectively [54,70,71]. As shown in Fig. 9, all scavengers resulted in less efficiencies for the PCO of o-xylene and acetaldehyde. In Fig. 9a, the degradation efficiency of 0.5NaFe-MOX for o-xylene decreased from 47.7% to 41.2%, 32.9% on trapping $\cdot\text{O}_2^-$ and $\cdot\text{OH}$, respectively. In Fig. 9b, the degradation efficiency of 1NaFe-MOX for acetaldehyde decreased from 38.0% to 0.00%, 25.4% on trapping $\cdot\text{O}_2^-$ and $\cdot\text{OH}$, respectively. The results indicated that $\cdot\text{O}_2^-$ and $\cdot\text{OH}$ were co-participated the photocatalytic degradation of o-xylene and

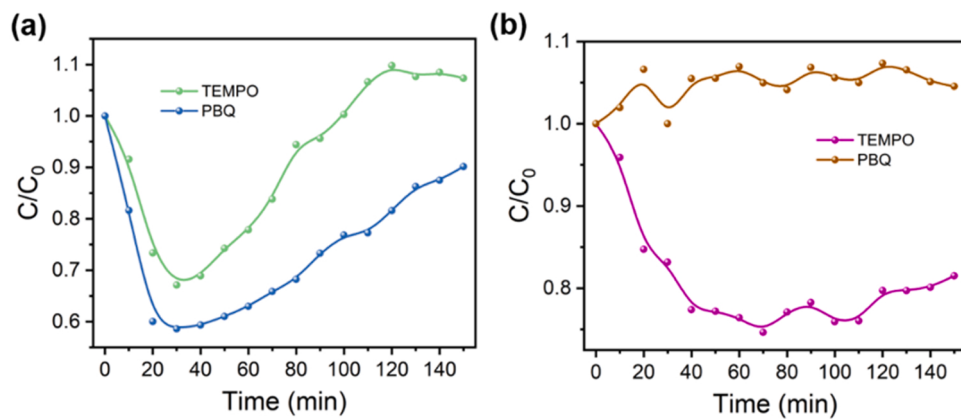


Fig. 9. *In-situ* trapping experiments of $\cdot\text{OH}$ (TEMPO) and $\cdot\text{O}_2$ (p-BQ) during 0.5NaFe-MOX and 1NaFe-MOX photocatalytic degradation of (a) o-xylene and (b) acetaldehyde.

acetaldehyde.

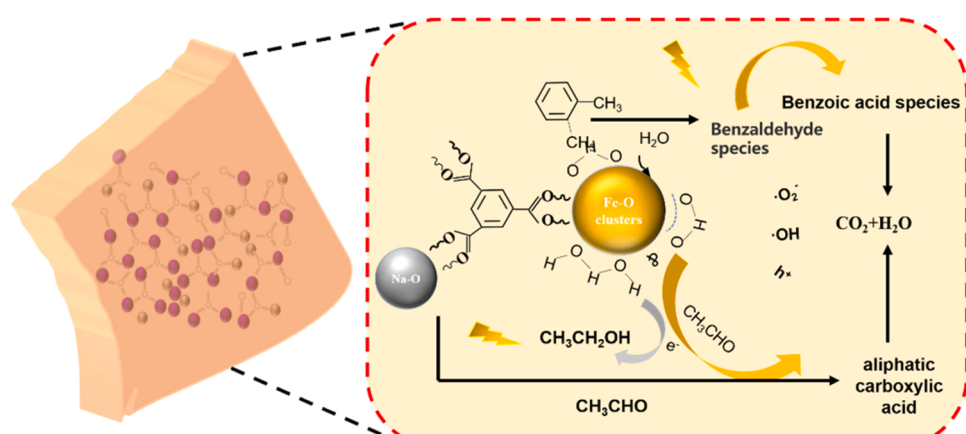
Besides, the tests of adding scavengers during the *in-situ* DRIFT spectra experiments were carried out further to identify the photocatalytic reaction path. As shown in Fig. S13a, during the photocatalytic degradation of o-xylene by 0.5NaFe-MOX in the light stage, a strong vibration peak of 1680 cm^{-1} (benzyl aldehydes) was observed when TEMPO was used to capture $\cdot\text{OH}$. However, in Fig. S13b, the vibration peaks of 1665 cm^{-1} (benzyl aldehydes) and 1775 cm^{-1} (benzoic acids) were both found when p-BQ was applied to capture $\cdot\text{O}_2$. This result indicated that $\cdot\text{O}_2$ promoted the conversion of o-xylene to benzyl aldehydes, while $\cdot\text{OH}$ further accelerated the conversion of benzyl aldehydes to benzoic acids, which was consistent with the results of *in-situ* trapping experiments for $\cdot\text{OH}$ and O_2 . As shown in Fig. S13c, during the photocatalytic degradation of acetaldehyde by 1NaFe-MOX in the light stage, a strong vibration peak of 1665 cm^{-1} (acetaldehyde) and a peak of 1770 cm^{-1} (aliphatic carboxylic acid) at 210 min was both observed when TEMPO was used to capture $\cdot\text{OH}$, while the vibration peaks of 1665 cm^{-1} (acetaldehyde) was only observed when p-BQ was applied to capture $\cdot\text{O}_2$ (Fig. S13d), confirming that O_2 was main active species to degrade acetaldehyde by 1NaFe-MOX.

From the kinetic studies and *in-situ* DRIFT spectra, the pathways of photocatalytic degradation of acetaldehyde and o-xylene by NaFe-MOXs were proposed in Scheme 2. Acetaldehyde molecules were adsorbed by NaFe-MOXs through both acetaldehyde-Fe interaction and H-bond. The acetaldehyde adsorbed through H-bond tended to convert to aliphatic carboxylic acid under the assistant of photo-induced holes, and finally be mineralized into CO_2 and H_2O by active oxygen radicals. O-xylene molecules, on the other way, were firstly adsorbed by the $\text{Fe}_3\text{O}(\text{OH})$

active sites in NaFe-MOX, which then attacked the α -H of adsorbed o-xylene to generate benzaldehyde species. The benzaldehyde species were further oxidized to benzoic acids in consecutive steps under the influence of Lewis acid/basic sites and reactive oxygen species. Finally, the benzoic acid was fully oxidized to CO_2 and H_2O .

4. Conclusion

Bimetallic NaFe-MOXs were successfully prepared by introducing $\text{C}_7\text{H}_5\text{NaO}_2$ into the synthesis system of MIL-100(Fe) MOX. The local charge imbalance of oxygen in carboxylic acid groups was engineered through the coordination between Na^+ , Fe^{3+} and BTC^{3-} to create the Lewis basic sites and achieve the adjustment of Lewis acid/basic sites in NaFe-MOXs. The Lewis acid sites of Fe-MOX enabled the effective adsorption of electron-rich aromatic VOCs (o-xylene), while the introduction of Lewis basic sites in NaFe-MOXs helped with the adsorption of electron-deficient oxygenated VOCs (acetaldehyde). Besides, the introduction of Lewis basic sites also promoted the adsorption of H_2O and the formation of $\cdot\text{OH}$ groups, which not only provided new H-bond interaction between carbonyl oxygen in acetaldehyde and $\cdot\text{OH}$ groups on NaFe-MOXs, but also facilitated the generation of more $\cdot\text{OH}$ radicals. Benefiting from the enhanced adsorption and new H-bond interaction, 1NaFe-MOX promoted the oxidation of acetaldehyde into aliphatic carboxylic acid and prevented the formation and accumulation of ethanol. Finally, compared with Fe-MOX, 0.5NaFe-MOX and 1NaFe-MOX showed improved mineralization ability in photocatalytic degradation of o-xylene and acetaldehyde. The successful preparation of the NaFe-MOXs provides a new synthetic approach for regulating the Lewis



Scheme 2. The proposed pathways of photocatalytic degradation of acetaldehyde and o-xylene by NaFe-MOXs.

acidity/basicity of the MOX materials to realize the controllable photocatalytic degradation of electron-rich aromatic and electron-deficient oxygenated VOCs.

CRediT authorship contribution statement

Lu Chen: Conceptualization, Investigation, Methodology, Formal analysis, Data curation, Writing-original draft. **Xiao Wang:** Conceptualization, Methodology, Resources, Funding acquisition, Project administration, Validation, Supervision, Writing-review & editing. **Gansheng Shi:** Formal analysis, Investigation. **Guanhong Lu:** Formal analysis, Investigation. **Yan Wang:** Formal analysis, Resources. **Xiaofeng Xie:** Formal analysis, Project administration. **Deliang Chen:** Formal analysis, Funding acquisition, Resources, Project administration. **Jing Sun:** Investigation, Validation, Funding acquisition, Resources, Project administration.

Declaration of Competing Interest

The authors declare no conflict of interest.

Data availability

Data will be made available on request.

Acknowledgment

This work was financially supported by National Natural Science Foundation of China (52072387), Natural Science Foundation of Shanghai (22ZR1471800), Shanghai Commission of Science and Technology Program (19DZ1202600, 20DZ1204100), National Natural Science Foundation of China (41907303, 51574205), the State Key Laboratory Director Fund of SICCAS (Y9ZC0102), Natural Science Foundation of Guangdong Province (2018B030311022), the Key Scientific Research Project in University of Henan Province (21A430040), Guangdong Basic and Applied Basic Research Foundation (2021B1515140047), Guangdong Provincial Key Construction Discipline Research Ability Enhancement Project (2021ZDJS090), and the Innovative Research Team (in Science and Technology) in University of Henan Province (19IRTSTHN028).

Appendix A. Supporting information

Supplementary data associated with this article can be found in the online version at [doi:10.1016/j.apcatb.2023.122850](https://doi.org/10.1016/j.apcatb.2023.122850).

References

- [1] J. Chen, L. Chen, X. Wang, Z. Rao, J. Sun, A. Chen, X. Xie, Rare-earth single atoms decorated 2D-TiO₂ nanosheets for the photodegradation of gaseous O-xylene, *J. Colloid Interface Sci.* 605 (2022) 674–684, <https://doi.org/10.1016/j.jcis.2021.07.129>.
- [2] B. Liu, J. Ji, B. Zhang, W. Huang, Y. Gan, D.Y.C. Leung, H. Huang, Catalytic ozonation of VOCs at low temperature: a comprehensive review, *J. Hazard. Mater.* 422 (2022), 126847, <https://doi.org/10.1016/j.jhazmat.2021.126847>.
- [3] Z. Wang, A. Mahmood, X. Xie, X. Wang, H. Qiu, J. Sun, Surface adsorption configurations of H₃PO₄ modified TiO₂ and its influence on the photodegradation intermediates of gaseous o-xylene, *Chem. Eng. J.* 393 (2020), 124723, <https://doi.org/10.1016/j.cej.2020.124723>.
- [4] M. Wen, G. Li, H. Liu, J. Chen, T. An, H. Yamashita, Metal-organic framework-based nanomaterials for adsorption and photocatalytic degradation of gaseous pollutants: recent progress and challenges, *Environ. Sci. Nano* 6 (2019) 1006–1025, <https://doi.org/10.1039/C8EN01167B>.
- [5] M. Humayun, H. Ullah, Z.-E. Cheng, A.A. Tahir, W. Luo, C. Wang, Au surface plasmon resonance promoted charge transfer in Z-scheme system enables exceptional photocatalytic hydrogen evolution, *Appl. Catal. B: Environ.* 310 (2022), 121322, <https://doi.org/10.1016/j.apcatb.2022.121322>.
- [6] H. Ullah, A.A. Tahir, T.K. Mallick, Structural and electronic properties of oxygen defective and Se-doped p-type BiVO₄(001) thin film for the applications of photocatalysis, *Appl. Catal. B: Environ.* 224 (2018) 895–903, <https://doi.org/10.1016/j.apcatb.2017.11.034>.
- [7] M. Humayun, H. Ullah, L. Shu, X. Ao, A.A. Tahir, C. Wang, W. Luo, Plasmon assisted highly efficient visible light catalytic CO₂ reduction over the noble metal decorated Sr-incorporated g-C₃N₄, *Nanomicro Lett.* 13 (2021) 209, <https://doi.org/10.1007/s40820-021-00736-x>.
- [8] H. Ullah, A.A. Tahir, S. Bibi, T.K. Mallick, S.Z. Karazhanov, Electronic properties of β-TaON and its surfaces for solar water splitting, *Appl. Catal. B: Environ.* 229 (2018) 24–31, <https://doi.org/10.1016/j.apcatb.2018.02.001>.
- [9] T. Grant Glover, G.W. Peterson, B.J. Schindler, D. Britt, O. Yaghi, MOF-74 building unit has a direct impact on toxic gas adsorption, *Chem. Eng. Sci.* 66 (2011) 163–170, <https://doi.org/10.1016/j.ces.2010.10.002>.
- [10] J.H. Fu, Z. Zhong, D. Xie, Y.J. Guo, D.X. Kong, Z.X. Zhao, M. Li, SERS-active MIL-100(Fe) sensory array for ultrasensitive and multiplex detection of VOCs, *Angew. Chem. Int. Ed.* 59 (2020) 20489–20498, <https://doi.org/10.1002/anie.202002720>.
- [11] M. Humayun, L. Shu, W. Pi, H. Xia, A. Khan, Z. Zheng, Q. Fu, Y. Tian, W. Luo, Vertically grown CeO₂ and TiO₂ nanoparticles over the MIL53Fe MOF as proper band alignments for efficient H₂ generation and 2,4-DCP degradation, *Environ. Sci. Pollut. Res.* 29 (2022) 34861–34873, <https://doi.org/10.1007/s11356-022-18684-3>.
- [12] X. Xu, Q. Deng, H.-C. Chen, M. Humayun, D. Duan, X. Zhang, H. Sun, X. Ao, X. Xue, A. Nikiforov, K. Huo, C. Wang, Y. Xiong, Metal-organic frameworks offering tunable binary active sites toward highly efficient urea oxidation electrolysis, *Research* (2022), <https://doi.org/10.34133/2022/9837109>.
- [13] V.I. Isaeva, M.D. Vedenyapina, S.A. Kulaishin, A.A. Lobova, V.V. Chernyshev, G. I. Kapustin, O.P. Tkachenko, V.V. Vergun, D.A. Arkhipov, V.D. Nissenbaum, L. M. Kustov, Adsorption of 2,4-dichlorophenoxyacetic acid in an aqueous medium on nanoscale MIL-53(Al) type materials, *Dalton Trans.* 48 (2019) 15091–15104, <https://doi.org/10.1039/C9DT03037A>.
- [14] H. Chang, Y. Zhou, S. Zhang, X. Zheng, Q. Xu, CO₂-induced 2D Ni-BDC metal-organic frameworks with enhanced photocatalytic CO₂ reduction activity, *Adv. Mater. Interfaces* 8 (2021), 2100205, <https://doi.org/10.1002/admi.202100205>.
- [15] P.M. Bhatt, V. Guillerm, S.J. Datta, A. Shkurenko, M. Eddaoudi, Topology meets reticular chemistry for chemical separations: MOFs as a case study, *Chem* 6 (2020) 1613–1633, <https://doi.org/10.1016/j.chempr.2020.06.018>.
- [16] J.R.L. Hong-Cai Zhou, M. Omar, Yaghi, Introduction to metal-organic frameworks, *Chem. Rev.* 112 (2012) 673–674, <https://doi.org/10.1021/cr300014x>.
- [17] E. Barea, C. Montoro, J.A.R. Navarro, Toxic gas removal-metal-organic frameworks for the capture and degradation of toxic gases and vapours, *Chem. Soc. Rev.* 43 (2014) 5419–5430, <https://doi.org/10.1039/C3CS60475F>.
- [18] K. Ge, S. Sun, Y. Zhao, K. Yang, S. Wang, Z. Zhang, J. Cao, Y. Yang, Y. Zhang, M. Pan, L. Zhu, Facile synthesis of two-dimensional iron/cobalt metal-organic framework for efficient oxygen evolution electrocatalysis, *Angew. Chem. Int. Ed.* 60 (2021) 12097–12102, <https://doi.org/10.1002/anie.202102632>.
- [19] S.C. Qi, X.Y. Qian, Q.X. He, K.J. Miao, Y. Jiang, P. Tan, X.Q. Liu, L.B. Sun, Generation of hierarchical porosity in metal-organic frameworks by the modulation of cation valence, *Angew. Chem. Int. Ed.* 58 (2019) 10104–10109, <https://doi.org/10.1002/anie.201903323>.
- [20] Y. Keum, B. Kim, A. Byun, J. Park, Synthesis and photocatalytic properties of titanium-porphyrinic aerogels, *Angew. Chem. Int. Ed.* 59 (2020) 21591–21596, <https://doi.org/10.1002/anie.202007193>.
- [21] R.K. Motkuri, H.V.R. Annareddy, M. Vijaykumar, H.T. Schaef, P.F. Martin, B. P. McGrail, L.X. Dang, R. Krishna, P.K. Thallapally, Fluorocarbon adsorption in hierarchical porous frameworks, *Nat. Commun.* 5 (2014) 4368, <https://doi.org/10.1038/ncomms5368>.
- [22] J. Hou, A.F. Sapnik, T.D. Bennett, Metal-organic framework gels and monoliths, *Chem. Sci.* 11 (2020) 310–323, <https://doi.org/10.1039/C9SC04961D>.
- [23] J. Zhang, C.-Y. Su, Metal-organic gels: from discrete metallo gelators to coordination polymers, *Coord. Chem. Rev.* 257 (2013) 1373–1408, <https://doi.org/10.1016/j.ccr.2013.01.005>.
- [24] J.K. Wychowanicz, H. Saini, B. Scheibe, D.P. Dubal, A. Schneemann, K. Jayaramulu, Hierarchical porous metal-organic gels and derived materials: from fundamentals to potential applications, *Chem. Soc. Rev.* 51 (2022) 9068–9126, <https://doi.org/10.1039/D2CS00585A>.
- [25] Z. Yang, X. Fu, L. Zhou, J. Yang, T. Deng, J. Chen, Y. Wen, X. Fu, D. Shen, Z. Yuan, Z. Du, S. Luo, C. Yu, Chem-inspired synthesis of injectable metal-organic hydrogels for programmable drug carriers, hemostasis and synergistic cancer treatment, *Chem. Eng. J.* 423 (2021), 130202, <https://doi.org/10.1016/j.cej.2021.130202>.
- [26] Y. Li, Z.W. Jiang, S.Y. Xiao, C.Z. Huang, Y.F. Li, Terbium(III) organic gels: novel antenna effect-induced enhanced electrochemiluminescence emitters, *Anal. Chem.* 90 (2018) 12191–12197, <https://doi.org/10.1021/acs.analchem.8b03383>.
- [27] A. Mahmood, W. Xia, N. Mahmood, Q. Wang, R. Zou, Hierarchical heteroaggregation of binary metal-organic gels with tunable porosity and mixed valence metal sites for removal of dyes in water, *Sci. Rep.* 5 (2015), 10556, <https://doi.org/10.1038/srep10556>.
- [28] S. Barman, J. Anand Garg, O. Blacque, K. Venkatesan, H. Berke, Triptycene based luminescent metal-organic gels for chemosensing, *Chem. Commun.* 48 (2012) 11127–11129, <https://doi.org/10.1039/C2CC34430K>.
- [29] L. Li, S. Xiang, S. Cao, J. Zhang, G. Ouyang, L. Chen, C.Y. Su, A synthetic route to ultralight hierarchically micro/mesoporous Al(III)-carboxylate metal-organic aerogels, *Nat. Commun.* 4 (2013) 1774, <https://doi.org/10.1038/ncomms2757>.
- [30] S. Saha, G. Das, J. Thote, R. Banerjee, Photocatalytic metal-organic framework from CdS quantum dot incubated luminescent metallohydrogel, *J. Am. Chem. Soc.* 136 (2014) 14845–14851, <https://doi.org/10.1021/ja509019k>.

- [31] X. Zheng, W. He, S. Rehman, P. Zhang, Facile synthesis of hydrophobic metal-organic gels for volatile organic compound capture, *ACS Appl. Mater. Interfaces* 12 (2020) 41359–41367, <https://doi.org/10.1021/acsmi.0c10818>.
- [32] X. Zheng, H. Zhang, S. Rehman, P. Zhang, Energy-efficient capture of volatile organic compounds from humid air by granular metal organic gel, *J. Hazard. Mater.* 411 (2021), 125057, <https://doi.org/10.1016/j.jhazmat.2021.125057>.
- [33] J.W. Yoon, Y.K. Seo, Y.K. Hwang, J.S. Chang, H. Leclerc, S. Wuttke, P. Bazin, A. Vimont, M. Daturi, E. Bloch, P.L. Llewellyn, C. Serre, P. Horcajada, J. M. Greneche, A.E. Rodrigues, G. Ferey, Controlled reducibility of a metal-organic framework with coordinatively unsaturated sites for preferential gas sorption, *Angew. Chem. Int. Ed.* 49 (2010) 5949–5952, <https://doi.org/10.1002/anie.201001230>.
- [34] L. Chen, X. Wang, Z. Rao, Z. Tang, G. Shi, Y. Wang, G. Lu, X. Xie, D. Chen, J. Sun, One-pot synthesis of the MIL-100 (Fe) MOF/MOX homojunctions with tunable hierarchical pores for the photocatalytic removal of BTXS, *Appl. Catal. B: Environ.* 303 (2022), 120885, <https://doi.org/10.1016/j.apcatb.2021.120885>.
- [35] T. Wang, Y. Wang, M. Sun, A. Hanif, H. Wu, Q. Gu, Y.S. Ok, D.C.W. Tsang, J. Li, J. Yu, J. Shang, Thermally treated zeolitic imidazolate framework-8 (ZIF-8) for visible light photocatalytic degradation of gaseous formaldehyde, *Chem. Sci.* 11 (2020) 6670–6681, <https://doi.org/10.1039/DOSC01397H>.
- [36] Y.C. Tan, H.C. Zeng, Lewis basicity generated by localised charge imbalance in noble metal nanoparticle-embedded defective metal-organic frameworks, *Nat. Commun.* 9 (2018) 4326, <https://doi.org/10.1038/s41467-018-06828-4>.
- [37] L. Hou, J.P. Zhang, X.M. Chen, S.W. Ng, Two highly-connected, chiral, porous coordination polymers featuring novel heptanuclear metal carboxylate clusters, *Chem. Commun.* (2008) 4019–4021, <https://doi.org/10.1039/B809069F>.
- [38] M. Huang, S. Gong, C. Wang, Y. Yang, P. Jiang, P. Wang, L. Hu, Q. Chen, Lewis-basic EDTA as a highly active molecular electrocatalyst for CO₂ reduction to CH₄, *Angew. Chem. Int. Ed.* 60 (2021) 23002–23009, <https://doi.org/10.1002/anie.202110594>.
- [39] M. Kong, W. Wei, W. Wang, H. Chen, J. He, A novel metal organic gel with superior oxidase-like activity for efficient and sensitive chemiluminescence detection of uric acid, *Spectrochim. Acta A Mol. Biomol. Spectrosc.* 257 (2021), 119773, <https://doi.org/10.1016/j.saa.2021.119773>.
- [40] D.S. Raja, J.-H. Luo, C.-T. Yeh, Y.-C. Jiang, K.-F. Hsu, C.-H. Lin, Novel alkali and alkaline earth metal coordination polymers based on 1,4-naphthalenedicarboxylic acid: synthesis, structural characterization and properties, *CrystEngComm* 16 (2014) 1985–1994, <https://doi.org/10.1039/C3CE42208A>.
- [41] Q. Xia, H. Wang, B. Huang, X. Yuan, J. Zhang, J. Zhang, L. Jiang, T. Xiong, G. Zeng, State-of-the-art advances and challenges of iron-based metal organic frameworks from attractive features, synthesis to multifunctional applications, *Small* 15 (2019), e1803088, <https://doi.org/10.1002/smll.201803088>.
- [42] F. Yu, X.-J. Kong, Y.-Y. Zheng, Y.-P. Ren, L.-S. Long, R.-B. Huang, L.-S. Zheng, pH-dependent assembly of OD to 3D Keggin-based coordination polymers: structures and catalytic properties, *Dalton Trans.* (2009) 9503–9509, <https://doi.org/10.1039/B911606K>.
- [43] P. Horcajada, S. Surble, C. Serre, D.Y. Hong, Y.K. Seo, J.S. Chang, J.M. Greneche, I. Margiolaki, G. Ferey, Synthesis and catalytic properties of MIL-100(Fe), an iron (III) carboxylate with large pores, *Chem. Commun.* (2007) 2820–2822, <https://doi.org/10.1039/B704325B>.
- [44] J. Zhou, Y. Dou, X.Q. Wu, A. Zhou, L. Shu, J.R. Li, Alkali-etched Ni(II)-based metal-organic framework nanosheet arrays for electrocatalytic overall water splitting, *Small* 16 (2020), e1906564, <https://doi.org/10.1002/smll.201906564>.
- [45] H. Jing, L. Chen, S. Yi, T. Li, J. Sun, D. Chen, Comparative insight into effect of hybridizing potassium and hydrogen ions on photocatalytic reduction/oxidation behavior of g-C₃N₄ nanocrystals, *Chem. Eng. J.* 417 (2021), 129187, <https://doi.org/10.1016/j.cej.2021.129187>.
- [46] F.F. Chen, K. Huang, Y. Zhou, Z.Q. Tian, X. Zhu, D.J. Tao, D.E. Jiang, S. Dai, Multi-molar absorption of CO₂ by the activation of carboxylate groups in amino acid ionic liquids, *Angew. Chem. Int. Ed.* 55 (2016) 7166–7170, <https://doi.org/10.1002/anie.201602919>.
- [47] N.-Y. Topsøe, K. Pedersen, E.G. Derouane, Infrared and temperature-programmed desorption study of the acidic properties of ZSM-5-type zeolites, *J. Catal.* 70 (1981) 41–52, [https://doi.org/10.1016/0021-9517\(81\)90315-8](https://doi.org/10.1016/0021-9517(81)90315-8).
- [48] M.L. Aubrey, B.M. Wiers, S.C. Andrews, T. Sakurai, S.E. Reyes-Lillo, S.M. Hamed, C.-J. Yu, L.E. Darago, J.A. Mason, J.-O. Baeg, F. Grandjean, G.J. Long, S. Seki, J. B. Neaton, P. Yang, J.R. Long, Electron delocalization and charge mobility as a function of reduction in a metal-organic framework, *Nat. Mater.* 17 (2018) 625–632, <https://doi.org/10.1038/s41563-018-0098-1>.
- [49] A.G. Hufnagel, K. Peters, A. Müller, C. Scheu, D. Fattakhova-Rohlfing, T. Bein, Zinc ferrite photoanode nanomorphologies with favorable kinetics for water-splitting, *Adv. Funct. Mater.* 26 (2016) 4435–4443, <https://doi.org/10.1002/adfm.201600461>.
- [50] S.-S. Yi, B.-R. Wulan, J.-M. Yan, Q. Jiang, Highly efficient photoelectrochemical water splitting: surface modification of cobalt-phosphate-loaded Co₃O₄/Fe₂O₃ p-n heterojunction nanorod arrays, *Adv. Funct. Mater.* 29 (2019), 1801902, <https://doi.org/10.1002/adfm.201801902>.
- [51] N. Tian, Y. Zhang, X. Li, K. Xiao, X. Du, F. Dong, G.J.N. Waterhouse, T. Zhang, H. Huang, Precursor-reforming protocol to 3D mesoporous g-C₃N₄ established by ultrathin self-doped nanosheets for superior hydrogen evolution, *Nano Energy* 38 (2017) 72–81, <https://doi.org/10.1016/j.nanoen.2017.05.038>.
- [52] C.H. Langford, J.H. Carey, The charge transfer photochemistry of the hexaaquoiron (III) ion, the chloropentaquoiron(III) ion, and the u-dihydroxo dimer explored with tert-butyl alcohol scavenging, *Can. J. Chem.* 53 (1975) 2430–2435, <https://doi.org/10.1139/v75-344>.
- [53] Y. Yao, G. Wu, F. Lu, S. Wang, Y. Hu, J. Zhang, W. Huang, F. Wei, Enhanced photo-Fenton-like process over Z-scheme CoFe₂O₄/g-C₃N₄ heterostructures under natural indoor light, *Environ. Sci. Pollut. Res.* 23 (2016) 21833–21845, <https://doi.org/10.1007/s11356-016-7329-2>.
- [54] S. Fang, W. Zhang, K. Sun, T. Tong, A.I. Lim, J. Bao, Z. Du, Y. Li, Y.H. Hu, Critical role of tetracycline's self-promotion effects in its visible-light driven photocatalytic degradation over ZnO nanorods, *Chemosphere* 309 (2022), 136691, <https://doi.org/10.1016/j.chemosphere.2022.136691>.
- [55] D. Ma, L. Yang, Z. Sheng, Y. Chen, Photocatalytic degradation mechanism of benzene over ZnWO₄: revealing the synergistic effects of Na-doping and oxygen vacancies, *Chem. Eng. J.* 405 (2021), 126538, <https://doi.org/10.1016/j.cej.2020.126538>.
- [56] L. Ding, M. Li, Y. Zhao, H. Zhang, J. Shang, H. Zhong, H. Sheng, C. Chen, J. Zhao, The vital role of surface Brønsted acid/base sites for the photocatalytic formation of free-OH radicals, *Appl. Catal. B: Environ.* 266 (2020), 118634, <https://doi.org/10.1016/j.apcatb.2020.118634>.
- [57] J.J. Liu, Y.B. Shan, C.R. Fan, M.J. Lin, C.C. Huang, W.X. Dai, Encapsulating naphthalene in an electron-deficient MOF to enhance fluorescence for organic amines sensing, *Inorg. Chem.* 55 (2016) 3680–3684, <https://doi.org/10.1021/acs.inorgchem.6b00252>.
- [58] H. Wang, W.P. Lustig, J. Li, Sensing and capture of toxic and hazardous gases and vapors by metal-organic frameworks, *Chem. Soc. Rev.* 47 (2018) 4729–4756, <https://doi.org/10.1039/C7CS00885F>.
- [59] A. Mahmood, G. Shi, X. Xie, J. Sun, Assessing the adsorption and photocatalytic activity of TiO₂ nanoparticles for the gas phase acetaldehyde: a computational and experimental study, *J. Alloy. Compd.* 819 (2020), 153055, <https://doi.org/10.1016/j.jallcom.2019.153055>.
- [60] S. Weon, W. Choi, TiO₂ nanotubes with open channels as deactivation-resistant photocatalyst for the degradation of volatile organic compounds, *Environ. Sci. Technol.* 50 (2016) 2556–2563, <https://doi.org/10.1021/acs.est.5b05418>.
- [61] J. Kong, Z. Xiang, G. Li, T. An, Introduce oxygen vacancies into CeO₂ catalyst for enhanced coke resistance during photothermocatalytic oxidation of typical VOCs, *Appl. Catal. B: Environ.* 269 (2020), 118755, <https://doi.org/10.1016/j.apcatb.2020.118755>.
- [62] X. Chen, J.-J. Li, X. Chen, S.-C. Cai, E.-Q. Yu, J. Chen, H. Jia, MOF-templated approach for Hollow NiO_x/Co₃O₄ catalysts: enhanced light-driven thermocatalytic degradation of toluene, *ACS Appl. Nano Mater.* 1 (2018) 2971–2981, <https://doi.org/10.1021/acsami.8b00587>.
- [63] R. Mi, D. Li, Z. Hu, R.T. Yang, Morphology effects of CeO₂ nanomaterials on the catalytic combustion of toluene: a combined kinetics and diffuse reflectance infrared fourier transform spectroscopy study, *ACS Catal.* 11 (2021) 7876–7889, <https://doi.org/10.1021/acscatal.1c01981>.
- [64] J. Wang, J. Li, W. Yang, Y. Liu, H. Wang, Q. Geng, F. Dong, Promote reactants activation and key intermediates formation for facilitated toluene photodecomposition via Ba active sites construction, *Appl. Catal. B: Environ.* 297 (2021), 120489, <https://doi.org/10.1016/j.apcatb.2021.120489>.
- [65] M.D. Hernández-Alonso, I. Tejedor-Tejedor, J.M. Coronado, M.A. Anderson, Operando FTIR study of the photocatalytic oxidation of methylcyclohexane and toluene in air over TiO₂-ZrO₂ thin films: Influence of the aromaticity of the target molecule on deactivation, *Appl. Catal. B: Environ.* 101 (2011) 283–293, <https://doi.org/10.1016/j.apcatb.2010.09.029>.
- [66] J. Li, Xa Dong, G. Zhang, W. Cui, W. Cen, Z. Wu, S.C. Lee, F. Dong, Probing ring-opening pathways for efficient photocatalytic toluene decomposition, *J. Mater. Chem. A* 7 (2019) 3366–3374, <https://doi.org/10.1039/C8TA11627J>.
- [67] Z. Rao, G. Lu, A. Mahmood, G. Shi, X. Xie, J. Sun, Deactivation and activation mechanism of TiO₂ and rGO/Er³⁺-TiO₂ during flowing gaseous VOCs photodegradation, *Appl. Catal. B: Environ.* 284 (2021), 119813, <https://doi.org/10.1016/j.apcatb.2020.119813>.
- [68] Z. Rao, X. Xie, X. Wang, A. Mahmood, S. Tong, M. Ge, J. Sun, Defect chemistry of Er³⁺-doped TiO₂ and its photocatalytic activity for the degradation of flowing gas-phase VOCs, *J. Phys. Chem. C* 123 (2019) 12321–12334, <https://doi.org/10.1021/acs.jpcc.9b02093>.
- [69] M. Xu, W. Wang, M. Hunger, Formation of acetone enol on acidic zeolite ZSM-5 evidenced by H/D exchange, *Chem. Commun.* (2003) 722–723, <https://doi.org/10.1039/B212701F>.
- [70] Y. Zhu, S. Fang, S. Chen, Y. Tong, C. Wang, Y.H. Hu, Highly efficient visible-light photocatalytic ethane oxidation into ethyl hydroperoxide as a radical reservoir, *Chem. Sci.* 12 (2021) 5825–5833, <https://doi.org/10.1039/D1SC00694K>.
- [71] Z. Rao, G. Lu, L. Chen, A. Mahmood, G. Shi, Z. Tang, X. Xie, J. Sun, Photocatalytic oxidation mechanism of gas-phase VOCs: unveiling the role of holes, OH and O₂⁻, *Chem. Eng. J.* 430 (2022), 132766 <https://doi.org/10.1016/j.cej.2021.132766>.